Active wetting of epithelial tissues

Carlos Pérez-González[#], Ricard Alert[#], Carles Blanch-Mercader, Manuel Gómez-González, Tomasz Kolodziej, Elsa Bazellieres, Jaume Casademunt*, Xavier Trepat*

[#] These authors contributed equally to this work

Affiliations:

[1] *Institute for Bioengineering of Catalonia, Barcelona 08028, Spain*

[2]*Facultat de Medicina, University of Barcelona, 08028 Barcelona, Spain*

[3]*Departament de Física de la Matèria Condensada, Facultat de Física, University of Barcelona, 08028 Barcelona, Spain*

[4]*University of Barcelona Institute of Complex Systems (UBICS), 08028 Barcelona, Spain*

[5]*Laboratoire Physico Chimie Curie, Institut Curie, PSL Research University - Sorbonne Universités, UPMC CNRS, UMR 168, 26 rue d'Ulm, F-75248 Paris Cedex 05, France*

[6]*Department of Biochemistry and NCCR Chemical Biology, Sciences II, University of Geneva, Quai Ernest-Ansermet 30, Geneva, CH-1211, Switzerland*

[7]*Faculty of Physics, Astronomy and Applied Computer Science, Jagiellonian University in Kraków, 30-348 Kraków, Poland*

[8]*Institució Catalana de Recerca i Estudis Avançats (ICREA), Barcelona, Spain.*

[9]*Centro de Investigación Biomédica en Red en Bioingeniería, Biomateriales y Nanomedicina, 08028, Spain*

correspondence to: jaume.casademunt@ub.edu (JC) and xtrepat@ibecbarcelona.eu (XT)

SUPPLEMENTARY MATERIAL

This document contains:

Supplementary note

Supplementary figures S1 to S16

Movies S1 to S11

SUPPLEMENTARY NOTE

A. Active polar fluid model of epithelial spreading

Instead of formulating a model based on adhesion energies, similar to those previously proposed to describe tissue wetting[1], our aim is to see how the wetting transition arises from mechanical models of collective cell migration. To this end, we extend a previously introduced continuum model of epithelial spreading[2] to the present problem. This continuum model takes a coarse-grained approach that describes the long-time and large-scale dynamics of the tissue as those of an active polar liquid, namely in terms of a polarity field $\boldsymbol{p}(\boldsymbol{r},t)$ and a flow field $\boldsymbol{v}(\boldsymbol{r},t)$. Below, we briefly justify this description, which has already been applied to the spreading of tissue monolayers[2–5]. A very similar model was also proposed for traction force and velocity profiles of single crawling cells[6].

1. Polarity dynamics

In our monolayer, cells at the center exert weak and random traction forces. In contrast, cells at the edge extend large lamellipodia towards the outside and exert strong inward-pointing traction forces on the substrate, indicating that they are polarized (Fig. 1h, Supplementary Fig. 3). The outwards polarization of cells at the border is likely due to contact inhibition of locomotion, a cell-cell interaction whereby cells repolarize in opposite directions upon contact[7,8]. In fact, this interaction is mediated by cell-cell adhesion, with front-rear differences in cadherin-based junctions acting as a cue for the repolarization[9–14]. Although originally proposed for mesenchymal cells, contact inhibition of locomotion is being increasingly recognized to play a key role in orchestrating the collective migration of epithelial monolayers[7,12–19]. In a cohesive monolayer, this interaction naturally leads to polarization of cells at the edge towards free space, leaving the inner region of the monolayer unpolarized. Such a polarity profile, in turn, explains the localization of traction forces at the edge and the build-up of tension at the center of epithelial monolayers[17,18]. Therefore, upon the expression of E-cadherin, we expect the polarity field $\boldsymbol{p}(\boldsymbol{r},t)$ to be set by an autonomous cellular mechanism such as contact inhibition of locomotion, which polarizes cells within a time scale $\tau_{\mathrm{CIL}} \sim 10$ min[11,19]. Hence, $\boldsymbol{p}(\boldsymbol{r},t)$ should remain essentially independent of flows in the monolayer, which occur over a longer time scale given by the strain rate, at least of order $\tau_s \sim 100$ min[2,20]. Consequently, within a phenomenological approach, we propose the polarity field to follow a purely relaxational dynamics given by

$$\frac{\partial p_\alpha}{\partial t} = -\frac{1}{\gamma_1}\frac{\delta F}{\delta p_\alpha}, \tag{S1}$$

where $F[\boldsymbol{p}]$ is the coarse-grained free energy functional of the orientational degrees of freedom, and γ_1 is a kinetic coefficient (the rotational viscosity for the angular degrees of freedom). With respect to the most general dynamics of the polarity field in an active polar fluid, Eq. (S1) neglects polarity advection and corotation, as well as flow alignment and active spontaneous polarization effects.

Then, since the bulk of the monolayer remains mechanically unpolarized, the coarse-grained free energy F includes a Landau expansion around the isotropic state $\boldsymbol{p} = 0$, and gradient terms resulting from nematic elasticity[21]:

$$F = \int_V \left[\frac{a}{2}p_\alpha p_\alpha + \frac{K}{2}\left(\partial_\alpha p_\beta\right)\left(\partial_\alpha p_\beta\right)\right] d^3\boldsymbol{r}, \tag{S2}$$

where $a > 0$ is a restoring coefficient of the polarity, and K is the Frank elastic constant in the usual

one-constant approximation. The dynamics of the polarity is thus given by

$$\partial_t p_\alpha = \frac{1}{\gamma_1}\left(-a p_\alpha + K\nabla^2 p_\alpha\right). \tag{S3}$$

In the limit of fast polarity dynamics compared to the spreading dynamics, the polarity field is always at equilibrium, $\partial_t p_\alpha = 0$, adiabatically adapting to the shape of the monolayer. Under this approximation, the polarity field is given by

$$L_c^2 \nabla^2 p_\alpha = p_\alpha, \tag{S4}$$

where we have defined the characteristic length $L_c \equiv \sqrt{K/a}$ of the polar order in the monolayer.

2. *Force balance*

Flows in cell monolayers occur at very low Reynolds numbers. Therefore, inertial forces are negligible, and hence momentum conservation reduces to the force balance condition

$$0 = \partial_\beta\left(\sigma^s_{\alpha\beta} + \sigma^a_{\alpha\beta} + \sigma^{E,s}_{\alpha\beta}\right) + f_\alpha, \tag{S5}$$

where $\sigma^s_{\alpha\beta}$ and $\sigma^a_{\alpha\beta}$ are the symmetric and antisymmetric parts of the deviatoric stress tensor, and f_α is the external force density. Respectively, $\sigma^{E,s}_{\alpha\beta}$ is the symmetric part of the Ericksen tensor. This tensor generalizes the pressure P to include anisotropic elastic stresses associated to the orientational degrees of freedom in liquid crystals[21]:

$$\sigma^E_{\alpha\beta} = -P\delta_{\alpha\beta} - \frac{\partial f}{\partial\left(\partial_\beta p_\gamma\right)}\partial_\alpha p_\gamma, \tag{S6}$$

where f is the Frank free energy density, namely the integrand of Eq. (S2). Thus, the orientational contribution to the Ericksen tensor is of second order in gradients of the polarity field, and hence we neglect it, so that force balance reads

$$0 = -\partial_\alpha P + \partial_\beta\left(\sigma^s_{\alpha\beta} + \sigma^a_{\alpha\beta}\right) + f_\alpha. \tag{S7}$$

Then, the pressure is related to the cell number surface density ρ by the equation of state of the monolayer. For the sake of an estimate, we assume the simplest form for an equation of state, $P(\rho) = B(\rho - \rho_0)/\rho_0$, where B is the bulk modulus of the monolayer, and ρ_0 is a reference density defined by $P(\rho_0) = 0$. Taking the pressure origin at the monolayer edge, $\rho_0 \sim 3\cdot 10^3$ cells/mm^2 (Supplementary Fig. 10). Respectively, density differences in the monolayer are, at most, $\rho - \rho_0 \sim 10^3$ cells/mm^2 (Supplementary Fig. 10). Then, the monolayer is expected to be highly compressible because area changes can in principle be accommodated by changes in height, resisted only by the shear modulus of the tissue. Hence, we estimate the bulk modulus of the monolayer by typical shear moduli of cell aggregates, which are in the range $G \sim 10^2 - 10^3$ Pa[22–24]. Thus, the pressure in the monolayer should be $P \lesssim 30 - 300$ Pa. In fact, isotropic compressive stresses (pressures) of ~ 50 Pa were shown to induce cell extrusion[25]. In conlusion, if tissue spreading is not dominated by cell proliferation[26–28], the magnitude of the pressure in the monolayer is expected to be much smaller than the tensile stress (tension) induced by traction forces, as measured by monolayer stress microscopy, which is of the order of several kPa (Fig. 1i), with a monolayer height of $h \sim 5$ μm. Hence, we neglect the pressure in the force balance:

$$0 = \partial_\beta\left(\sigma^s_{\alpha\beta} + \sigma^a_{\alpha\beta}\right) + f_\alpha. \tag{S8}$$

Now, for a nematic medium, the antisymmetric part of the stress tensor is given by $\sigma^a_{\alpha\beta} = 1/2\,(p_\alpha h_\beta - h_\alpha p_\beta)$, where $h_\alpha = -\delta F/\delta p_\alpha$ is the molecular field. From Eq. (S1), the adiabatic approximation for the polarity dynamics, $\partial_t p_\alpha = 0$, implies $h_\alpha = 0$. Therefore, the antisymmetric part of the stress tensor vanishes under this approximation, $\sigma^a_{\alpha\beta} = 0$. Thus, force balance reduces to

$$0 = \partial_\beta \sigma^s_{\alpha\beta} + f_\alpha. \tag{S9}$$

Finally, multiplying Eq. (S9) by the height $h(t)$ of the monolayer, the force balance can be rewritten in terms of the experimentally measured traction stress $T_\alpha(\boldsymbol{r}, t)$ and monolayer tension $\sigma_{\alpha\beta}(\boldsymbol{r}, t)$ fields:

$$\partial_\beta \sigma_{\alpha\beta} = T_\alpha, \tag{S10}$$

from where

$$T_\alpha = -f_\alpha h, \qquad \sigma_{\alpha\beta} = \sigma^s_{\alpha\beta} h. \tag{S11}$$

3. *Constitutive equations*

Next, constitutive equations must be given to specify the deviatoric stress tensor $\sigma^s_{\alpha\beta}$ and the external force f_α in terms of the polarity and velocity fields. The generic constitutive equations of an active liquid crystal are provided by active gel theory[29–32]. Here, based on the previous assumptions for the dynamics of the polarity field, we propose a simplified version of the generic constitutive equations of an active polar gel to describe epithelial spreading.

First, the spreading occurs on timescales of the order of $\tau_s \sim 100$ min[2], at which the tissue should have a fluid rheology. This time scale is much slower than the turnover time scales of proteins in the cytoskeleton or in cell-cell junctions, which are of the order of tens of minutes at most[33,34]. Intra- or intercellular processes such as cytoskeletal reorganizations or cell-cell slidings dissipate energy over these time scales, so that elastic energy may only be stored in the tissue at shorter times. Therefore, to describe the slow spreading dynamics, we will not consider the elastic response of the tissue at short time scales. Note that incessant cell-cell sliding and neighbour exchanges are observed throughout the experiments (Supplementary Movie 7), which provides further support to the fluid behaviour of the monolayer at the experimentally relevant time scales.

Then, in the viscous limit, the constitutive equations for the internal stress and the interfacial force of an active polar medium are:

$$\sigma^s_{\alpha\beta} = 2\eta\tilde{v}_{\alpha\beta} + \frac{\nu_1}{2}\left(p_\alpha h_\beta + h_\alpha p_\beta - \frac{2}{d} p_\gamma h_\gamma \delta_{\alpha\beta}\right) - \zeta q_{\alpha\beta} + \left(\bar{\eta}\, d\, v_{\gamma\gamma} + \bar{\nu}_1\, d\, p_\gamma h_\gamma - \bar{\zeta} - \zeta' p_\gamma p_\gamma\right)\delta_{\alpha\beta}, \tag{S12}$$

$$f_\alpha = -\xi v_\alpha + \nu_i \dot{p}_\alpha + \zeta_i p_\alpha, \tag{S13}$$

where, $q_{\alpha\beta} = p_\alpha p_\beta - p_\gamma p_\gamma/d\ \delta_{\alpha\beta}$ is the traceless symmetric nematic order parameter tensor, with d the system dimensionality, and v_α is the velocity of the fluid with respect to the substrate. The coefficients η and $\bar{\eta}$ are the shear and bulk viscosities of the medium, ζ is the anisotropic active stress coefficient, and $\bar{\zeta}$ and ζ' are two isotropic active stress coefficients. Finally, ξ, ν_i, and ζ_i are the corresponding interfacial versions of the viscosity (viscous friction), flow alignment (polar friction), and active stress (active force) coefficients. The constitutive equation for the internal stress, Eq. (S12), is that of an active polar gel with a variable modulus of the polarity[30]. In turn, the constitutive equation for the

interfacial force, Eq. (S13), is less conventional[35], but it was derived from a mesoscopic model of an active polar gel[36].

Now, the adiabatic approximation for the polarity dynamics implies $\dot{p}_\alpha = h_\alpha = 0$, so that flow alignment terms contribute neither to the stress tensor nor to the interfacial force. Next, we assume that polarized cells generate much larger active stresses than unpolarized cells. Hence, we neglect the active stress coefficient $\bar{\zeta}$ in front of ζ and ζ'. Note that, to capture the wetting transition with a model for a two-dimensional fluid layer, the fluid must be compressible, meaning that bulk coefficients must be retained. Then, for simplicity, we assume $\zeta = \zeta' d = 2\zeta'$ and $2\eta = \bar{\eta} d = 2\bar{\eta}$. Under these simplifications, the constitutive equations reduce to

$$\sigma^s_{\alpha\beta} = \eta \left(\partial_\alpha v_\beta + \partial_\beta v_\alpha\right) - \zeta p_\alpha p_\beta, \tag{S14}$$

$$f_\alpha = -\xi v_\alpha + \zeta_i p_\alpha, \tag{S15}$$

which close the set of equations defining the active polar fluid model of the spreading of an epithelial monolayer.

B. Traction and flow profiles

In this section, the model is solved in a circular geometry. There are two unknown fields: the polarity field $\boldsymbol{p}(\boldsymbol{r}, t)$ and the flow field $\boldsymbol{v}(\boldsymbol{r}, t)$. The polarity field is completely specified by Eq. (S4). Once the polarity profile is known, introducing the constitutive equations Eqs. (S14) and (S15) into the force balance condition Eq. (S9) sets a closed equation for the flow field. The equations for both the polarity and the flow field are time-independent. Therefore, the time dependence of these fields arises solely from the boundary conditions at the free interface, which moves according to $dR/dt = v_r(R)$.

1. *Traction profile*

Since traction forces are mainly along the radial direction (Fig. 1h, Supplementary Fig. 3), we assume the polarity field to be radial: $\boldsymbol{p} = p(r)\,\boldsymbol{r}$. Hence, in polar coordinates, Eq. (S4) reads

$$r^2 p''(r) + r p'(r) - \left[1 + \frac{r^2}{L_c^2}\right] p(r) = 0. \tag{S16}$$

Because of the strong outwards polarization of cells at the edge of the cell island, we impose $p(R) = 1$, namely the maximal polarity value, as a boundary condition. Finitude and symmetry of the profile also require $p(0) = 0$. Hence, the solution for the radial polarity profile is

$$p(r) = \frac{I_1(r/L_c)}{I_1(R/L_c)}, \tag{S17}$$

where I_1 is the modified Bessel function of the first kind and first order. Therefore, the nematic length L_c characterizes the decay of the tissue polarity from its maximal value at the boundary towards its vanishing value in the bulk (red gradient in Fig. 3a).

Next, we may compare the two sources of dissipation, the viscosity and the friction coefficient, whose ratio defines the hydrodynamic screening length $\lambda = \sqrt{\eta/\xi}$. For monolayers smaller than this length, $R < \lambda$, viscosity dominates over friction, and the monolayer stress profile features a central plateau of maximal stress. In contrast, for monolayers larger than this length, $R > \lambda$, friction

dominates over viscosity, and the monolayer stress decays at the center, thus featuring its maximum close to the monolayer edge[2]. In our case, the stress is always maximal at the center of the monolayer (Fig. 1i), meaning that $R > \lambda$. Hence, we neglect cell-substrate friction hereafter. This corresponds to the so-called wet limit, $\lambda \to \infty$, in which the flows in the monolayer are fully hydrodynamically coupled, with no screening effects due to the release of stress to the substrate through friction[31]. In this limit, the force balance reduces to

$$\partial_\beta \sigma_{\alpha\beta} = -T_0 p_\alpha, \tag{S18}$$

where we have defined the active traction stress coefficient $T_0 = \zeta_i h$, which gives the maximal traction stress exerted at the edge of the monolayer.

Then, we fit the predicted radial traction force profile $T_r(r) = -T_0 p(r)$ to the experimentally measured profiles at different times, as represented in kymographs as in Supplementary Fig. 3a (see Fig. 3d and Methods). From the fits, we obtain the time evolution of the maximal traction stress $T_0(t)$ and the nematic length $L_c(t)$ (Fig. 3e, f). After an initial transient, the nematic length remains essentially constant throughout the experiment (Fig. 3f), taking a value $L_c \sim 25$ μm. This gives support to the assumption that the polarity field is set by a flow-independent mechanism, and that its dynamics is quasi-static.

Now, by combining the inferred value of the nematic length L_c with estimates for typical traction forces and cell migration velocities, we can estimate all the parameters of the polarity dynamics, namely the rotational viscosity γ_1, the restoring force coefficient a, and the Frank elastic constant K. To this end, we start by estimating the cell-substrate friction coefficient as $\xi \sim T/(vh)$. Taking typical values of traction stresses $T \sim 100$ Pa and speeds $v \sim 10$ μm/min for cell migration[26], and estimating the cell height $h \sim 5$ μm (Supplementary Fig. 4), we get $\xi \sim 100$ Pa·s/μm^2, consistent with previous estimates[37]. Then, we assume that the rotational viscosity mainly arises from the friction between the substrate and polarized cytoskeletal structures such as the lamellipodia[3]. Thus, considering the polarized structures to be rods of length $\ell \sim 10$ μm comparable to cell length, the rotational friction may be estimated as $\gamma_1 \sim \xi \ell^2 \sim 10$ kPa·s. Now, together with the restoring force coefficient a, the rotational friction γ_1 determines the time scale of the polarity field: $\tau_p \sim \gamma_1/a$. As argued above, the polarity field should be essentially set by contact inhibition of locomotion interactions, so that the time scale of the polarity field may be estimated by that of contact inhibition events, $\tau_p \sim \tau_{\mathrm{CIL}} \sim 10$ min[11,19]. This gives an estimate for the polarity restoring force coefficient $a \sim 20$ Pa. Finally, we estimate the Frank constant as $K = aL_c^2 \sim 10$ nN. The estimates of model parameters are collected in Table I.

Finally, knowing the value of K allows to check that the orientational contribution of the Ericken tensor in Eq. (S6) is negligible as argued above. Using Eq. (S2) and the polarity profile in Eq. (S17), this contribution can be estimated as $K(p')^2 \sim K/L_c^2 = a \sim 20$ Pa. Therefore, it is much smaller than the typical tensile stresses measured in the monolayer, of the order of several kPa, and it can be safely neglected.

2. *Flow profile*

The next step is to solve the force balance equation to obtain the velocity field. As for the traction field, we also consider a radial velocity field, $\boldsymbol{v} = v(r)\,\boldsymbol{r}$. Thus, in polar coordinates, the nonvanishing components of the stress tensor are

$$\frac{1}{h}\sigma_{rr} = \eta v' - \zeta p^2, \qquad \frac{1}{h}\sigma_{\theta\theta} = \eta \frac{v}{r}, \tag{S19}$$

Symbol	Description	Estimate
h	monolayer height	$5\ \mu$m
ξ	friction coefficient	100 Pa·s/μm^2
T_0	maximal traction	$0.2-0.8$ kPa
L_c	nematic length	$25\ \mu$m
$-\zeta$	contractility	$5-50$ kPa
γ_1	rotational viscosity	10 kPa·s
a	polarity restoring coefficient	20 Pa
K	Frank constant	10 nN
η	monolayer viscosity	$3-30$ MPa·s
λ	hydrodynamic screening length	$0.2-0.6$ mm
D	noise intensity of monolayer shape fluctuations	$0.05-1.5\ \mu$m^2/h

Table I. Estimates of model parameters.

and the force balance reads

$$\sigma'_{rr}+\frac{\sigma_{rr}-\sigma_{\theta\theta}}{r}=-T_0 p. \tag{S20}$$

Hence, the equation for the velocity profile is

$$\eta\left[v''+\frac{1}{r}v'-\frac{1}{r^2}v\right]=-\frac{T_0}{h}p+\zeta\left[\frac{1}{r}p^2+2pp'\right]. \tag{S21}$$

Finitude and symmetry of the velocity profile impose $v\left(0\right)=0$. In addition, in agreement with the experimental measurements, we impose normal stress-free boundary conditions at the tissue boundary: $n_\alpha\sigma_{\alpha\beta}n_\beta|_{r=R}=0$. This translates into $\sigma_{rr}\left(R\right)=0$, which is the same condition employed to compute the monolayer tension via monolayer stress microscopy. Under these conditions, the velocity profile reads

$$\begin{aligned}v\left(r\right)=\frac{1}{2\eta}\Bigg[\Bigg[\zeta-2T_0\frac{L_c^2}{hR}+\left[\zeta\frac{L_c}{R}+2T_0\frac{L_c}{h}\right]\frac{I_0\left(R/L_c\right)}{I_1\left(R/L_c\right)}-\zeta\frac{I_0^2\left(R/L_c\right)}{I_1^2\left(R/L_c\right)}\Bigg]r\\+\left[\zeta\frac{I_0\left(r/L_c\right)}{I_1\left(R/L_c\right)}-2T_0\frac{L_c}{h}\right]L_c\frac{I_1\left(r/L_c\right)}{I_1\left(R/L_c\right)}\Bigg],\end{aligned} \tag{S22}$$

which is plotted in Supplementary Fig. 9a (red curve).

Now, the previous solution is general for a freely spreading cell monolayer. However, the monolayers in our experiments are confined within circular adherent regions. In the wetting phase, this confinement imposes $v\left(R\right)=0$. With no integration constants left, this extra boundary condition sets a relationship between model parameters. Since the values of $T_0\left(t\right)$ and $L_c\left(t\right)$ are set by traction profiles, this condition directly determines the active stress coefficient $\zeta\left(t\right)$ in terms of the other parameters:

$$\zeta=-2T_0\frac{L_c}{h}\frac{I_2\left(R/L_c\right)}{I_1\left(R/L_c\right)-I_0\left(R/L_c\right)\left[\frac{I_0(R/L_c)}{I_1(R/L_c)}-\frac{2L_c}{R}\right]}. \tag{S23}$$

Thus, whereas all model parameters are free in a spreading or retracting monolayer, they are not independent in a confined monolayer. Equation (S23) shows that, under confinement, the active stress

coefficient is negative, hence corresponding to a so-called contractile active stress. Accordingly, the coefficient $-\zeta$ is called *contractility* hereinafter. During the dewetting phase, the confinement restriction is released, and hence the contractility becomes an independent parameter, not governed by Eq. (S23) anymore.

Both for confined and free monolayers, a general feature of the predicted velocity profiles is their nonmonotonicity (Supplementary Fig. 9a). The model predicts an outwards flow at a velocity that, close to the center, has a linearly increasing profile, with a slope controlled by traction forces: $v(r) \approx T_0 L_c/(\eta h)\, r; r \ll R$, as obtained from Eq. (S22) in the limit $L_c \ll R$. In contrast, through Eq. (S19), the stress-free boundary condition $\sigma_{rr}(R) = 0$ imposes the slope of the velocity at the boundary to be $v'(R) = \zeta/\eta < 0$. Hence, the contractility causes the velocity to drop at the peripheral polarized region of width L_c. Therefore, the velocity a bit behind the boundary is always higher than at the very boundary (Supplementary Fig. 9a). As a consequence, cells are expected to accumulate close to the monolayer edge as they flow outwards. Experimentally, a gradient of increasing cell density towards the edge develops in the monolayer (Supplementary Fig. 10), consistently with the predicted flow profile.

The increase in peripheral cell number density might promote the extrusion of live cells from the monolayer[38–40], eventually leading to the formation of 3D structures at the monolayer edge. This is indeed what seems to occur in our monolayers (Supplementary Fig. 4, Supplementary Movie 4). In fact, 3D structures in the form of cell rims were previously observed both in confined and unconfined monolayers[41,42]. We suggest that the formation of these structures might partially stem from the predicted flow-induced accumulation of cells at the tissue edge.

C. Critical size for tissue wetting

We now focus on deriving the wetting transition, defined by a vanishing spreading parameter, $S = 0$. The spreading parameter is directly related to the spreading velocity[43] $V = v(R)$ by $S = \eta V$, so that using Eq. (S22) it reads

$$S = \frac{\zeta R}{2} - 2\frac{T_0 L_c^2}{h} + \left[\zeta L_c + \frac{T_0 L_c R}{h}\right] \frac{I_0(R/L_c)}{I_1(R/L_c)} - \frac{\zeta R}{2}\frac{I_0^2(R/L_c)}{I_1^2(R/L_c)}. \tag{S24}$$

In the experimentally relevant limit $L_c \ll R$, it reduces to

$$S \approx \frac{T_0 L_c}{h} R + \left(\zeta - \frac{3T_0 L_c}{h}\right)\frac{L_c}{2}. \tag{S25}$$

This result gives the spreading parameter in terms of the active forces responsible for collective cell migration, showing that the wetting transition results from a competition between traction forces and tissue contractility. Thus, note that, in contrast to other studies of wetting phenomena in active liquid crystal films[44,45], our treatment of the wetting transition in tissues based on an active polar fluid model crucially accounts for active traction forces, which give rise to the distinct physics of the active wetting transition.

From Eq. (S24), monolayer dewetting will occur whenever the contractility exceed the critical value

$$-\zeta^* = 2T_0\frac{L_c}{h}\frac{I_2(R/L_c)}{I_1(R/L_c) - I_0(R/L_c)\left[\frac{I_0(R/L_c)}{I_1(R/L_c)} - \frac{2L_c}{R}\right]} \approx \frac{T_0}{h}(2R - 3L_c), \tag{S26}$$

which increases with the radius of the monolayer as shown in Fig. 3c. Therefore, larger monolayers require a higher contractility to induce the dewetting. This can be understood by looking at the

velocity profiles of monolayers of different radii. As explained above, traction forces at the edge impose a linearly increasing velocity profile at the central region of the monolayer. As a result, larger monolayers reach higher velocities right behind the narrow polarized peripheral region of width L_c (Supplementary Fig. 9b). In turn, the wetting transition condition imposes a vanishing velocity at the boundary. As also explained above, the contractility is responsible for the velocity drop across the strongly polarized peripheral layer. Thus, larger monolayers require a higher contractility to bring the velocity down to zero at the boundary.

Note that the critical contractility $-\zeta^*$ is precisely the contractility under confinement (Eq. (S23)), since confinement also imposes the condition $V = 0$ in the wetting phase. Therefore, while fully spread, our confined monolayers are in a resting state ($V = 0$) maintained by the parallel increase of traction $T_0(t)$ and contractility $-\zeta(t)$, continuously fulfilling Eq. (S26).

D. Morphological instability during monolayer dewetting

1. *Linear stability analysis*

In this section, we study the morphological stability of the retracting tissue front during monolayer dewetting. To allow for the loss of the circular tissue shape, we include the ortoradial components of the polarity and velocity fields. Thus, Eq. (S4) reads

$$\left(\partial_r^2 + \frac{1}{r}\partial_r - \frac{1}{r^2}\right) p_r + \frac{1}{r^2}\partial_\theta^2 p_r - \frac{2}{r^2}\partial_\theta p_\theta = \frac{1}{L_c^2} p_r, \tag{S27a}$$

$$\left(\partial_r^2 + \frac{1}{r}\partial_r - \frac{1}{r^2}\right) p_\theta + \frac{1}{r^2}\partial_\theta^2 p_\theta + \frac{2}{r^2}\partial_\theta p_r = \frac{1}{L_c^2} p_\theta. \tag{S27b}$$

Force balance is expressed as

$$\frac{1}{r}\partial_r\left(r\sigma^s_{rr}\right) + \frac{1}{r}\partial_\theta \sigma^s_{\theta r} - \frac{1}{r}\sigma^s_{\theta\theta} = -T_0/h\, p_r, \tag{S28a}$$

$$\frac{1}{r}\partial_r\left(r\sigma^s_{r\theta}\right) + \frac{1}{r}\partial_\theta \sigma^s_{\theta\theta} + \frac{1}{r}\sigma^s_{\theta r} = -T_0/h\, p_\theta, \tag{S28b}$$

with the components of the stress tensor given by

$$\sigma^s_{rr} = 2\eta\, \partial_r v_r - \zeta p_r^2, \tag{S29a}$$

$$\sigma^s_{r\theta} = \sigma^s_{\theta r} = \eta\left[r\partial_r\left(\frac{v_\theta}{r}\right) + \frac{1}{r}\partial_\theta v_r\right] - \zeta p_r p_\theta, \tag{S29b}$$

$$\sigma^s_{\theta\theta} = \frac{2\eta}{r}\left(v_r + \partial_\theta v_\theta\right) - \zeta p_\theta^2. \tag{S29c}$$

The solution for the unperturbed state, which preserves circular symmetry, is given by Eqs. (S17) and (S22):

$$p_r^0(r) = \frac{I_1(r/L_c)}{I_1(R_0/L_c)}, \tag{S30}$$

$$v_r^0(r) = \frac{1}{2\eta}\left[\left[\zeta - 2T_0\frac{L_c^2}{hR_0} + \left[\zeta\frac{L_c}{R_0} + 2T_0\frac{L_c}{h}\right]\frac{I_0(R_0/L_c)}{I_1(R_0/L_c)} - \zeta\frac{I_0^2(R_0/L_c)}{I_1^2(R_0/L_c)}\right] r \right.$$
$$\left. + \left[\zeta\frac{I_0(r/L_c)}{I_1(R_0/L_c)} - 2T_0\frac{L_c}{h}\right] L_c\frac{I_1(r/L_c)}{I_1(R_0/L_c)}\right], \tag{S31}$$

where the superindex indicates the zeroth order in the front perturbations, and R_0 is the monolayer radius, which changes according to $dR_0/dt = v_r^0(R_0)$.

Next, we introduce small-amplitude perturbations of the circular monolayer boundary (Fig. 5b):

$$R(\theta) = R_0 + \delta R(\theta). \tag{S32}$$

Then, the polarity and velocity fields are correspondingly perturbed:

$$p_r(r,\theta) = p_r^0(r) + \delta p_r(r,\theta), \qquad p_\theta(r,\theta) = \delta p_\theta(r,\theta), \tag{S33}$$

$$v_r(r,\theta) = v_r^0(r) + \delta v_r(r,\theta), \qquad v_\theta(r,\theta) = \delta v_\theta(r,\theta). \tag{S34}$$

To impose boundary conditions, we define the normal and tangential vectors at the boundary,

$$\boldsymbol{n} = \cos\alpha\, \boldsymbol{r} + \sin\alpha\, \boldsymbol{\theta} \approx \boldsymbol{r} - \frac{1}{R_0}\frac{d\delta R}{d\theta}\boldsymbol{\theta}, \tag{S35a}$$

$$\boldsymbol{t} = -\sin\alpha\, \boldsymbol{r} + \cos\alpha\, \boldsymbol{\theta} \approx \frac{1}{R_0}\frac{d\delta R}{d\theta}\boldsymbol{r} + \boldsymbol{\theta}, \tag{S35b}$$

where α is the angle between the normal directions of the perturbed and unperturbed interfaces. In terms of the normal and tangential vectors, the conditions that impose a normal and maximal polarity at the boundary read

$$\boldsymbol{p}\cdot\boldsymbol{n}|_{r=R} = 1, \qquad \boldsymbol{p}\cdot\boldsymbol{t}|_{r=R} = 0. \tag{S36}$$

For the radial component, these conditions imply $p_r(R) \approx 1$, which expands into

$$p_r(R) = p_r^0(R) + \delta p_r(R) \approx p_r^0(R_0) + \partial_r p_r^0(R_0)\,\delta R + \delta p_r(R) \approx 1, \tag{S37}$$

so that

$$\delta p_r(R) = -\partial_r p_r^0(R_0)\,\delta R. \tag{S38}$$

For the ortoradial component,

$$\delta p_\theta(R) = -\frac{1}{R_0}\frac{d\delta R}{d\theta}. \tag{S39}$$

In turn, the boundary conditions on the stress impose a vanishing normal and shear stress at the interface:

$$\boldsymbol{n}\cdot\boldsymbol{\sigma}\cdot\boldsymbol{n}|_{r=R} = 0, \qquad \boldsymbol{t}\cdot\boldsymbol{\sigma}\cdot\boldsymbol{n}|_{r=R} = 0. \tag{S40}$$

The condition on the normal stress gives $\sigma_{rr}(R) = 0$ which, after expanding as previously, yields

$$\delta\sigma_{rr}(R) = -\partial_r\sigma_{rr}^0(R_0)\,\delta R. \tag{S41}$$

Finally, the condition on the shear stress imposes $\sigma_{r\theta}(R) = 0$, which translates into

$$\delta\sigma_{r\theta}(R) = \frac{1}{R_0}\frac{d\delta R}{d\theta}\sigma_{\theta\theta}^0(R_0) = \frac{2\eta}{hR_0^2}v_r^0(R_0)\frac{d\delta R}{d\theta}. \tag{S42}$$

Next, we decompose the perturbations in their Fourier modes, identified by an index n (Fig. 5b):

$$\delta R\left(\theta,t\right)=\sum_{n=0}^{\infty}\delta\tilde{R}_{n}\left(t\right)e^{in\theta}, \tag{S43a}$$

$$\delta p_{\alpha}\left(r,\theta,t\right)=\sum_{n=0}^{\infty}\delta\tilde{p}_{\alpha,n}\left(r,t\right)e^{in\theta}, \tag{S43b}$$

$$\delta v_{\alpha}\left(r,\theta,t\right)=\sum_{n=0}^{\infty}\delta\tilde{v}_{\alpha,n}\left(r,t\right)e^{in\theta}. \tag{S43c}$$

In terms of the Fourier modes, the equations for the polarity components read

$$\left(\partial_{r}^{2}+\frac{1}{r}\partial_{r}-\frac{1+n^{2}}{r^{2}}-\frac{1}{L_{c}^{2}}\right)\delta\tilde{p}_{r}=\frac{2in}{r^{2}}\delta\tilde{p}_{\theta}, \tag{S44a}$$

$$\left(\partial_{r}^{2}+\frac{1}{r}\partial_{r}-\frac{1+n^{2}}{r^{2}}-\frac{1}{L_{c}^{2}}\right)\delta\tilde{p}_{\theta}=-\frac{2in}{r^{2}}\delta\tilde{p}_{r}. \tag{S44b}$$

In turn, the components of the force balance, once the constitutive equation has been introduced, are expressed as

$$\begin{aligned}&2\eta\left(\partial_{r}^{2}+\frac{1}{r}\partial_{r}-\frac{1+n^{2}/2}{r^{2}}\right)\delta\tilde{v}_{r}+\frac{in\eta}{r}\left(\partial_{r}-\frac{3}{r}\right)\delta\tilde{v}_{\theta}\\&\quad+\left[T_{0}/h-2\zeta\left(\left(\partial_{r}+\frac{1}{r}\right)p_{r}^{0}+p_{r}^{0}\partial_{r}\right)\right]\delta\tilde{p}_{r}-\frac{in\zeta}{r}p_{r}^{0}\delta\tilde{p}_{\theta}=0,\end{aligned} \tag{S45a}$$

$$\begin{aligned}&\frac{in\eta}{r}\left(\partial_{r}+\frac{3}{r}\right)\delta\tilde{v}_{r}+\eta\left(\partial_{r}^{2}+\frac{1}{r}\partial_{r}-\frac{1+2n^{2}}{r^{2}}\right)\delta\tilde{v}_{\theta}\\&\quad+\left[T_{0}/h-\zeta\left(\left(\partial_{r}+\frac{2}{r}\right)p_{r}^{0}+p_{r}^{0}\partial_{r}\right)\right]\delta\tilde{p}_{\theta}=0.\end{aligned} \tag{S45b}$$

Finally, in Fourier space, the boundary conditions read

$$\delta\tilde{p}_{r,n}\left(R\right)=-\partial_{r}p_{r}^{0}\left(R_{0}\right)\delta\tilde{R}_{n},\qquad\delta\tilde{p}_{\theta,n}\left(R\right)=-\frac{in}{R_{0}}\delta\tilde{R}_{n}, \tag{S46}$$

$$\delta\tilde{\sigma}_{rr,n}\left(R\right)=-\partial_{r}\sigma_{rr}^{0}\left(R_{0}\right)\delta\tilde{R}_{n},\qquad\delta\tilde{\sigma}_{r\theta,n}\left(R\right)=\frac{2in\eta}{hR_{0}^{2}}v_{r}^{0}\left(R_{0}\right)\delta\tilde{R}_{n}. \tag{S47}$$

At this point, the four coupled ordinary differential equations Eqs. (S44) and (S45) are solved for $\delta\tilde{p}_{\alpha,n}\left(r\right)$ and $\delta\tilde{v}_{\alpha,n}\left(r\right)$. The solution is completely analytical for mode $n=0$ and almost analytical for the rest of modes, meaning that it has an analytical expression that involves two integrals that need to be numerically evaluated. Then, from the Fourier modes of the velocity field, the perturbed spreading velocity can be obtained as

$$V=\boldsymbol{v}\cdot\boldsymbol{n}|_{r=R}=\left[\boldsymbol{v}^{\,0}\cdot\boldsymbol{n}+\delta\boldsymbol{v}\cdot\boldsymbol{n}\right]_{r=R}\approx v_{r}^{0}\left(R_{0}\right)+\partial_{r}v_{r}^{0}\left(R_{0}\right)\delta R+\delta v_{r}\left(R_{0}\right), \tag{S48}$$

which implies

$$\delta V\left(\theta\right)=V\left(\theta\right)-V_{0}=\partial_{r}v_{r}^{0}\left(R_{0}\right)\delta R\left(\theta\right)+\delta v_{r}\left(R_{0},\theta\right). \tag{S49}$$

Thus, the growth rate ω_n of the tissue shape perturbations follows from

$$\delta\tilde{V}_n = \frac{1}{2\pi}\int_0^{2\pi} \delta V(\theta)\, e^{-in\theta} d\theta = \frac{d\delta\tilde{R}_n}{dt} = \omega_n \delta\tilde{R}_n. \tag{S50}$$

Hence,

$$\omega_n = \partial_r v_r^0(R_0) + \frac{\delta\tilde{v}_{r,n}(R_0)}{\delta\tilde{R}_n}. \tag{S51}$$

The resulting growth rate is a purely real number under any conditions, showing that there is no oscillatory instability. At the onset of dewetting, namely using typical critical parameter values T_0^*, L_c^*, and $-\zeta^*$ that define the tissue wetting transition (Fig. 4d, f; Supplementary Fig. 14), the cell monolayer exhibits a long-wavelength morphological instability (Fig. 5j). Several modes corresponding to deformations of the tissue shape ($n \geq 2$, Fig. 5b) are unstable. Hence, we propose that this instability is at the root of the observed shape changes during monolayer dewetting (Fig. 5a, Supplementary Movie 11).

2. *Monolayer viscosity*

At the wetting transition point, all the model parameters are known except for the monolayer viscosity. This allows us to estimate the monolayer viscosity at the wetting transition η^* from the retraction rate of the monolayer (Fig. 5e):

$$\begin{aligned}\omega_0 = \frac{1}{4\eta}\Bigg[2T_0\frac{R_0}{h} + 3\zeta + 2\Bigg[\zeta\left[\frac{L_c}{R_0} - \frac{R_0}{L_c}\right] + 2T_0\frac{L_c}{h}\Bigg]\frac{I_0(R_0/L_c)}{I_1(R_0/L_c)} \\ - \left[2T_0\frac{R_0}{h} + 5\zeta\right]\frac{I_0^2(R_0/L_c)}{I_1^2(R_0/L_c)} + 2\zeta\frac{R_0}{L_c}\frac{I_0^3(R_0/L_c)}{I_1^3(R_0/L_c)}\Bigg],\end{aligned} \tag{S52}$$

which is approximated by

$$\omega_0 \approx \frac{T_0 L_c}{2\eta h} \tag{S53}$$

in the limit $L_c \ll R_0$.

3. *Structure factor of monolayer shape*

To compute the structure factor, we add a noise term to the dynamics of the perturbation modes, Eq. (S50). Thus, the corresponding Langevin equation reads

$$\frac{d\delta\tilde{R}_n}{dt} = \omega_n \delta\tilde{R}_n + \tilde{\xi}_n(t). \tag{S54}$$

Assuming that shape fluctuations are fast compared to the dewetting dynamics, we consider that they are temporally uncorrelated and hence we take a Gaussian white noise:

$$\left\langle \tilde{\xi}_n(t) \right\rangle = 0, \qquad \left\langle \tilde{\xi}_n(t)\, \tilde{\xi}_m^*(t') \right\rangle = 2D\delta_{n,m}\delta(t-t'), \tag{S55}$$

where D is the noise intensity, which we assume independent of the mode number n. Now, under the approximation of a constant growth rate ω_n in the short time span $t_f - t^* = 7$ h, the solution to Eq. (S54) can be formally expressed as

$$\delta\tilde{R}_n(t) = \delta\tilde{R}_n(t^*)\, e^{\omega_n(t-t^*)} + e^{\omega_n t}\int_{t^*}^{t} \tilde{\xi}_n(t')\, e^{-\omega_n t'}\, dt'. \tag{S56}$$

Considering no shape perturbations at the onset of dewetting, $\delta\tilde{R}_n(t^*) = 0$, the equal-time structure factor reads

$$S_n(t) = \left\langle |\delta\tilde{R}_n(t)|^2 \right\rangle = e^{2\omega_n t}\int_{t^*}^{t}\int_{t^*}^{t} \left\langle \tilde{\xi}_n(t')\, \tilde{\xi}_n^*(t'') \right\rangle e^{-\omega_n(t'+t'')}\, dt'\, dt'' = \frac{D}{\omega_n}\left[e^{2\omega_n(t-t^*)} - 1\right], \tag{S57}$$

where we have employed Eq. (S55).

Finally, once the experimental value for ω_0 is known, the experimental growth rate is determined from the structure factor by numerically inverting the relation

$$\frac{S_n(t_f)}{S_0(t_f)} = \frac{\omega_0}{\omega_n}\frac{e^{2\omega_n(t_f-t^*)} - 1}{e^{2\omega_0(t_f-t^*)} - 1}, \tag{S58}$$

which is independent of the noise intensity D.

SUPPLEMENTARY REFERENCES

1. Douezan, S. *et al.* Spreading dynamics and wetting transition of cellular aggregates. *Proc. Natl. Acad. Sci. U. S. A.* **108**, 7315–20 (2011).
2. Blanch-Mercader, C. *et al.* Effective viscosity and dynamics of spreading epithelia: a solvable model. *Soft Matter* **13**, 1235–1243 (2017).
3. Lee, P. & Wolgemuth, C. W. Crawling Cells Can Close Wounds without Purse Strings or Signaling. *PLoS Comput. Biol.* **7**, e1002007 (2011).
4. Lee, P. & Wolgemuth, C. Advent of complex flows in epithelial tissues. *Phys. Rev. E* **83**, 061920 (2011).
5. Vig, D. K., Hamby, A. E. & Wolgemuth, C. W. Cellular Contraction Can Drive Rapid Epithelial Flows. *Biophys. J.* **113**, 1613–1622 (2017).
6. Roux, C. *et al.* Prediction of traction forces of motile cells. *Interface Focus* **6**, 20160042 (2016).
7. Mayor, R. & Carmona-Fontaine, C. Keeping in touch with contact inhibition of locomotion. *Trends Cell Biol.* **20**, 319–28 (2010).
8. Stramer, B. & Mayor, R. Mechanisms and in vivo functions of contact inhibition of locomotion. *Nat. Rev. Mol. Cell Biol.* **18**, 43–55 (2017).
9. Desai, R. A., Gao, L., Raghavan, S., Liu, W. F. & Chen, C. S. Cell polarity triggered by cell-cell adhesion via E-cadherin. *J. Cell Sci.* **122**, 905–11 (2009).
10. Khalil, A. A. & Friedl, P. Determinants of leader cells in collective cell migration. *Integr. Biol.* **2**, 568 (2010).
11. Weber, G. F., Bjerke, M. A. & DeSimone, D. W. A Mechanoresponsive Cadherin-Keratin Complex Directs Polarized Protrusive Behavior and Collective Cell Migration. *Dev. Cell* **22**, 104–15 (2012).
12. Theveneau, E. & Mayor, R. Collective cell migration of epithelial and mesenchymal cells. *Cell. Mol. Life Sci.* **70**, 3481–3492 (2013).
13. Vedula, S. R. K., Ravasio, A., Lim, C. T. & Ladoux, B. Collective cell migration: a mechanistic perspective. *Physiology* **28**, 370–9 (2013).
14. Ladoux, B., Mège, R.-M. & Trepat, X. Front-Rear Polarization by Mechanical Cues: From Single Cells to Tissues. *Trends Cell Biol.* **26**, 420–433 (2016).
15. Mayor, R. & Etienne-Manneville, S. The front and rear of collective cell migration. *Nat. Rev. Mol. Cell Biol.* **17**, 97–109 (2016).

16. Hakim, V. & Silberzan, P. Collective cell migration: a physics perspective. *Reports Prog. Phys.* **80**, 076601 (2017).
17. Zimmermann, J., Camley, B. A., Rappel, W.-J. & Levine, H. Contact inhibition of locomotion determines cell-cell and cell-substrate forces in tissues. *Proc. Natl. Acad. Sci. U. S. A.* **113**, 2660–2665 (2016).
18. Coburn, L. *et al.* Contact inhibition of locomotion and mechanical cross-talk between cell-cell and cell-substrate adhesion determine the pattern of junctional tension in epithelial cell aggregates. *Mol. Biol. Cell* **27**, 3436–3448 (2016).
19. Smeets, B. *et al.* Emergent structures and dynamics of cell colonies by contact inhibition of locomotion. *Proc. Natl. Acad. Sci. U. S. A.* **113**, 14621–14626 (2016).
20. Vincent, R. *et al.* Active Tensile Modulus of an Epithelial Monolayer. *Phys. Rev. Lett.* **115**, 248103 (2015).
21. de Gennes, P.-G. & Prost, J. *The Physics of Liquid Crystals* (Oxford University Press, 1993), 2nd edn.
22. Forgacs, G., Foty, R. A., Shafrir, Y. & Steinberg, M. S. Viscoelastic Properties of Living Embryonic Tissues: a Quantitative Study. *Biophys. J.* **74**, 2227–34 (1998).
23. Marmottant, P. *et al.* The role of fluctuations and stress on the effective viscosity of cell aggregates. *Proc. Natl. Acad. Sci. U. S. A.* **106**, 17271–5 (2009).
24. Guevorkian, K., Colbert, M.-J., Durth, M., Dufour, S. & Brochard-Wyart, F. Aspiration of Biological Viscoelastic Drops. *Phys. Rev. Lett.* **104**, 218101 (2010).
25. Saw, T. B. *et al.* Topological defects in epithelia govern cell death and extrusion. *Nature* **544**, 212–216 (2017).
26. Basan, M., Elgeti, J., Hannezo, E., Rappel, W.-J. & Levine, H. Alignment of cellular motility forces with tissue flow as a mechanism for efficient wound healing. *Proc. Natl. Acad. Sci. U. S. A.* **110**, 2452–9 (2013).
27. Recho, P., Ranft, J. & Marcq, P. One-dimensional collective migration of a proliferating cell monolayer. *Soft Matter* **12**, 2381–91 (2016).
28. Yabunaka, S. & Marcq, P. Cell growth, division, and death in cohesive tissues: A thermodynamic approach. *Phys. Rev. E* **96**, 022406 (2017).
29. Kruse, K., Joanny, J. F., Jülicher, F., Prost, J. & Sekimoto, K. Generic theory of active polar gels: a paradigm for cytoskeletal dynamics. *Eur. Phys. J. E* **16**, 5–16 (2005).
30. Jülicher, F. Active fluids and gels. In Ben Amar, M., Goriely, A., Müller, M. M. & Cugliandolo, L. (eds.) *New Trends in the Physics and Mechanics of Biological Systems*, chap. 4 (Oxford University Press, 2011).
31. Marchetti, M. C. *et al.* Hydrodynamics of soft active matter. *Rev. Mod. Phys.* **85**, 1143–1189 (2013).
32. Prost, J., Jülicher, F. & Joanny, J.-F. Active gel physics. *Nat. Phys.* **11**, 111–117 (2015).
33. Wyatt, T., Baum, B. & Charras, G. A question of time: tissue adaptation to mechanical forces. *Curr. Opin. Cell Biol.* **38**, 68–73 (2016).
34. Khalilgharibi, N., Fouchard, J., Recho, P., Charras, G. & Kabla, A. The dynamic mechanical properties of cellularised aggregates. *Curr. Opin. Cell Biol.* **42**, 113–120 (2016).
35. Jülicher, F. & Prost, J. Generic theory of colloidal transport. *Eur. Phys. J. E* **29**, 27–36 (2009).
36. Oriola, D., Alert, R. & Casademunt, J. Fluidization and Active Thinning by Molecular Kinetics in Active Gels. *Phys. Rev. Lett.* **118**, 088002 (2017).
37. Cochet-Escartin, O., Ranft, J., Silberzan, P. & Marcq, P. Border Forces and Friction Control Epithelial Closure Dynamics. *Biophys. J.* **106**, 65–73 (2014).
38. Eisenhoffer, G. T. *et al.* Crowding induces live cell extrusion to maintain homeostatic cell numbers in epithelia. *Nature* **484**, 546–9 (2012).
39. Marinari, E. *et al.* Live-cell delamination counterbalances epithelial growth to limit tissue overcrowding. *Nature* **484**, 542–5 (2012).
40. Eisenhoffer, G. T. & Rosenblatt, J. Bringing balance by force: live cell extrusion controls epithelial cell numbers. *Trends Cell Biol.* **23**, 185–192 (2013).
41. Deforet, M., Hakim, V., Yevick, H., Duclos, G. & Silberzan, P. Emergence of collective modes and tri-dimensional structures from epithelial confinement. *Nat. Commun.* **5**, 3747 (2014).
42. Kaliman, S., Jayachandran, C., Rehfeldt, F. & Smith, A.-S. Novel Growth Regime of MDCK II Model Tissues on Soft Substrates. *Biophys. J.* **106**, L25–8 (2014).
43. Beaune, G. *et al.* How cells flow in the spreading of cellular aggregates. *Proc. Natl. Acad. Sci. U. S. A.* **111**, 8055–8060 (2014).
44. Joanny, J.-F. & Ramaswamy, S. A drop of active matter. *J. Fluid Mech.* **705**, 46–57 (2012).
45. Joanny, J.-F., Kruse, K., Prost, J. & Ramaswamy, S. The actin cortex as an active wetting layer. *Eur. Phys.*

J. E **36**, 9866 (2013).

Supplementary figure S1

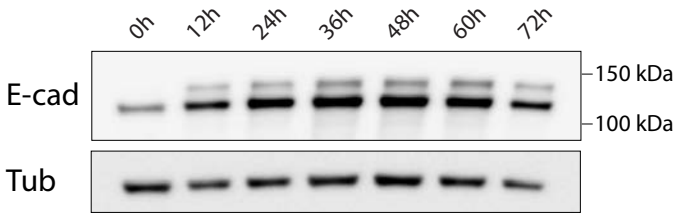

Fig. S1. E-cadherin western blot during 3 days of induction. E-cadherin increases in time during the first 24h and plateaus for at least 2 more days.

Supplementary figure S2

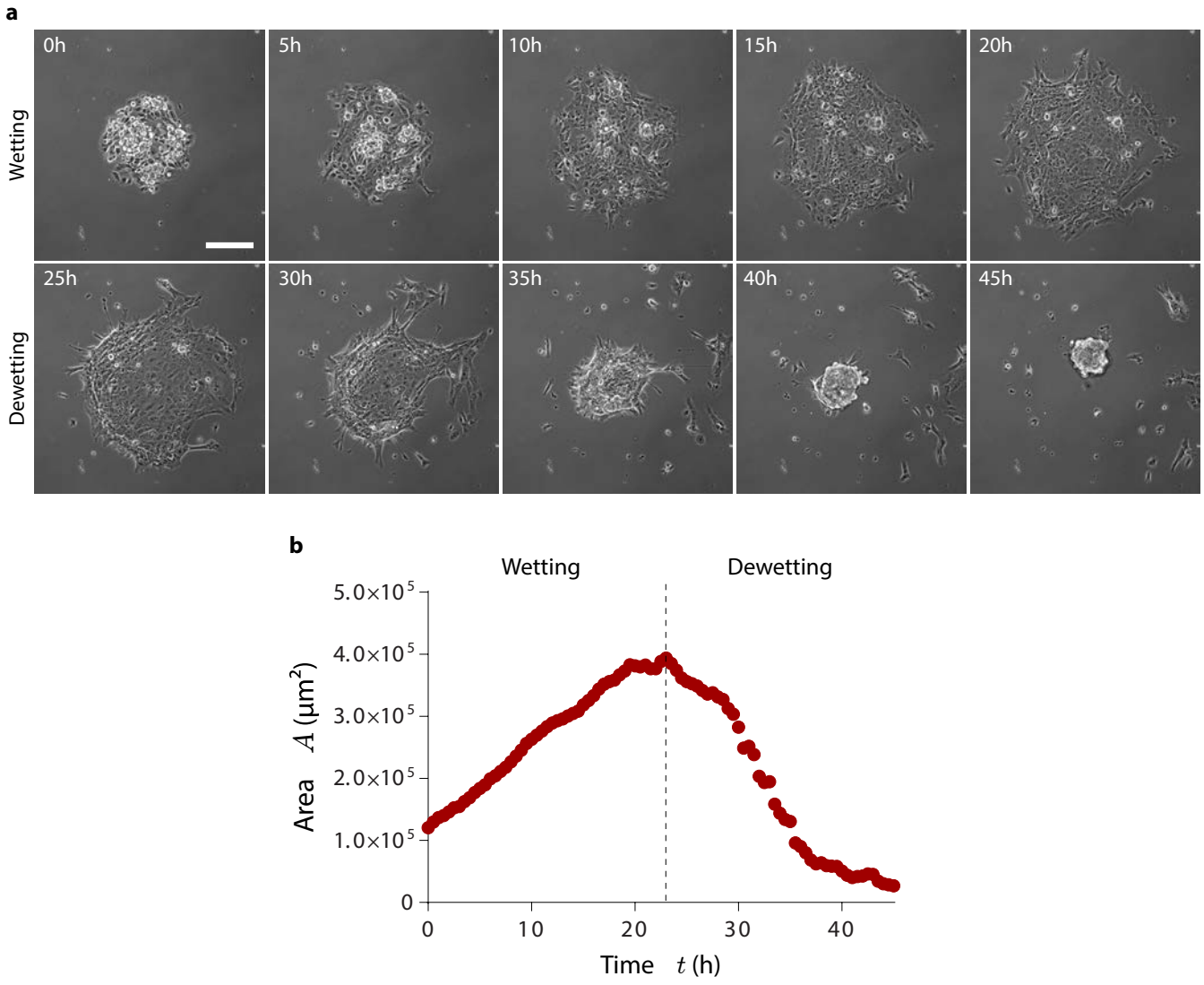

Fig. S2. Spreading cell monolayers exhibit a transition from wetting to dewetting. a-b, Phase contrast images (a) and time evolution of monolayer area (b) of a representative unconfined monolayer undergoing a transition between wetting ($\dot{A}>0$) and dewetting ($\dot{A}<0$) at time t=22h. Scale bar = 150 μm.

Supplementary figure S3

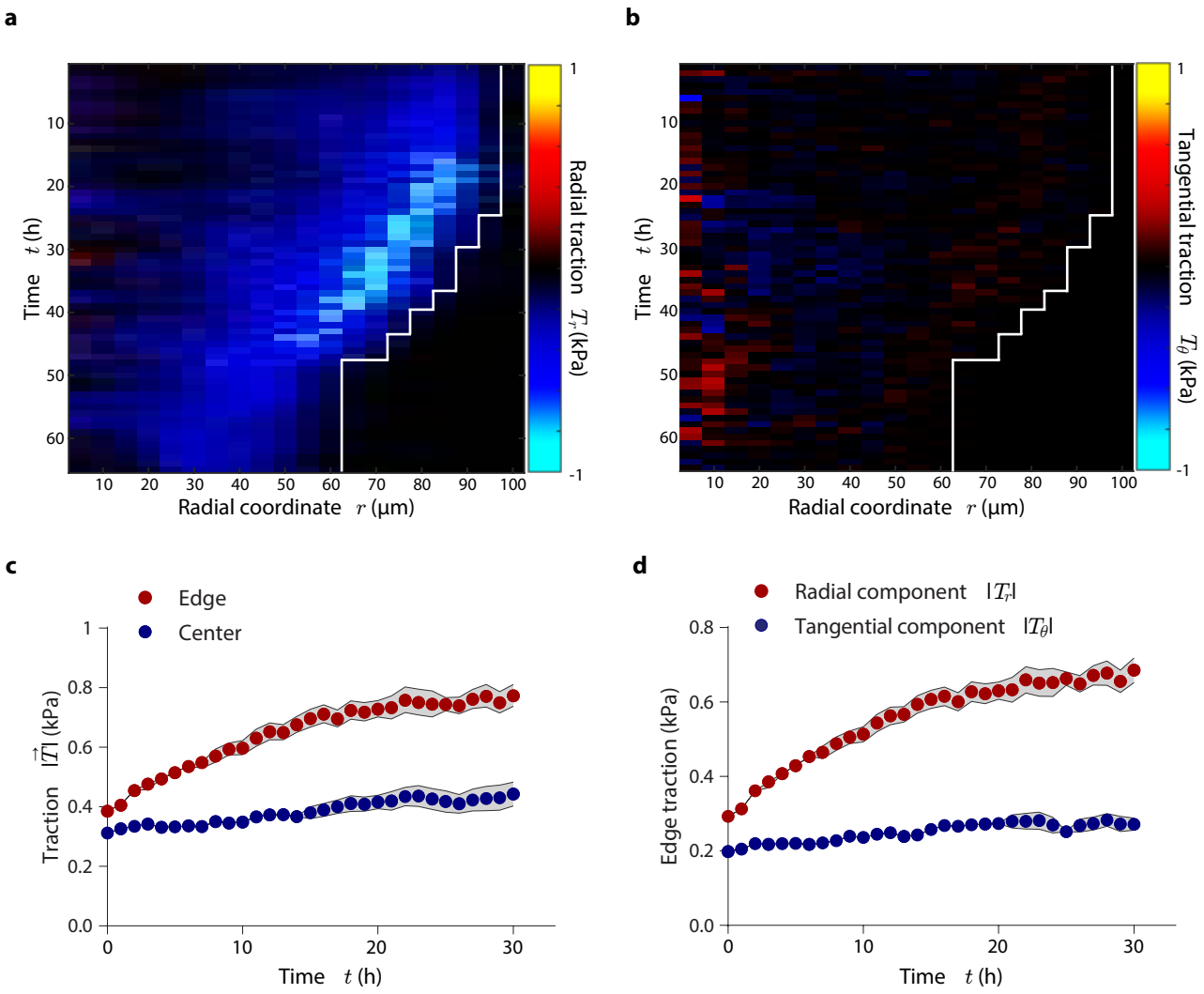

Fig. S3. Traction forces are primarily radial and accumulate at the edge of the monolayer upon E-cadherin expression. a-b, Kymographs of the radial (a) and tangential (b) components of the traction profile. **c**, Evolution of the traction magnitude at the monolayer edge and at the center. **d**, Evolution of the radial and tangential components of the traction at the edge of the monolayer. Data are presented as mean ± s.e.m. n=18 cell islands.

Supplementary figure S4

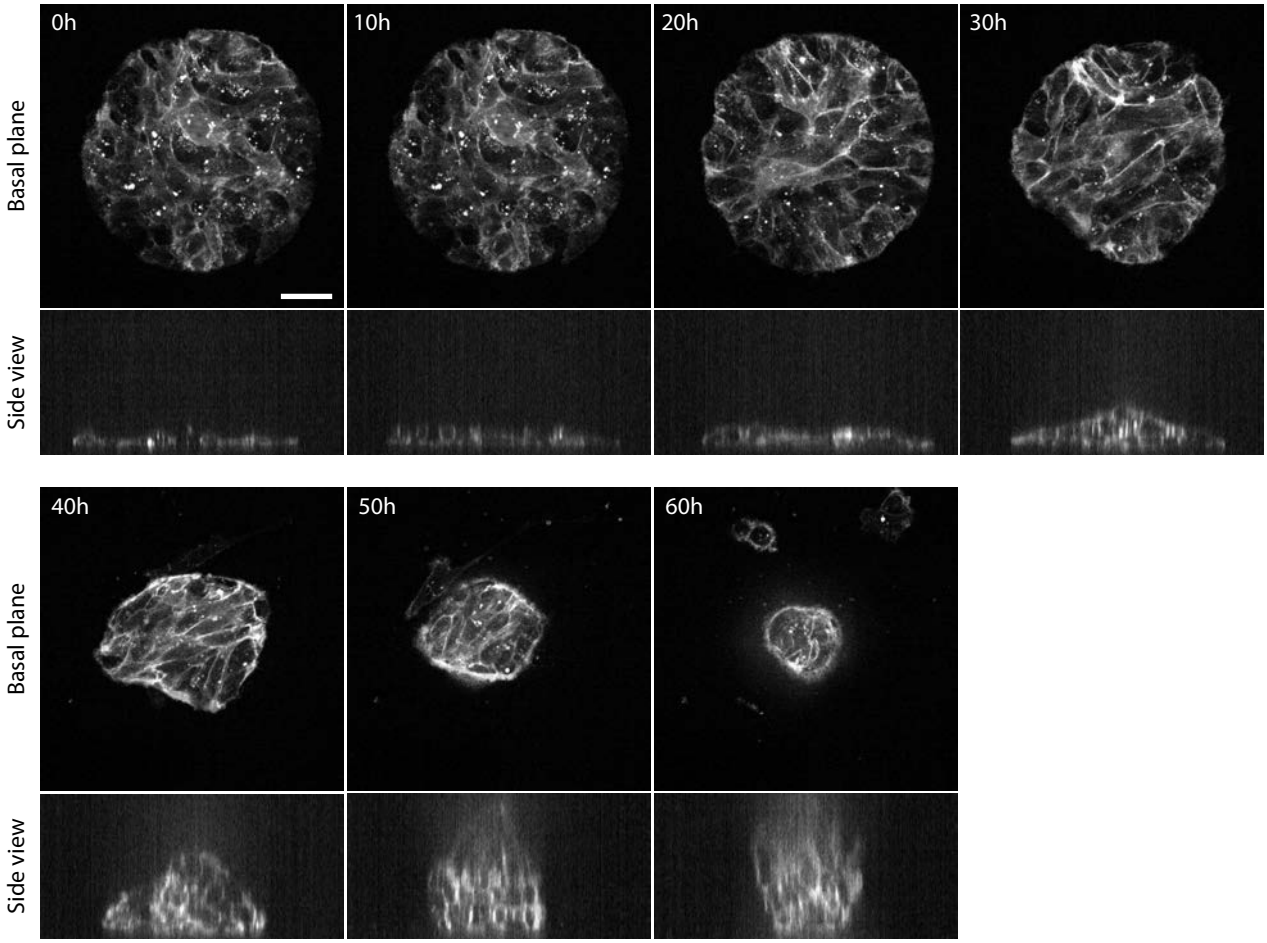

Fig. S4. Orthogonal views of monolayer dewetting. Life imaging of plasma membrane labelled cells (CAAX-iRFP) allow the visualization of tissue morphology in 3D. The tissue-substrate contact area decreases pronouncedly during dewetting, while the tissue evolves from a monolayer to a spheroidal cell aggregate, resembling a droplet. Scale bar = 40 μm.

Supplementary figure S5

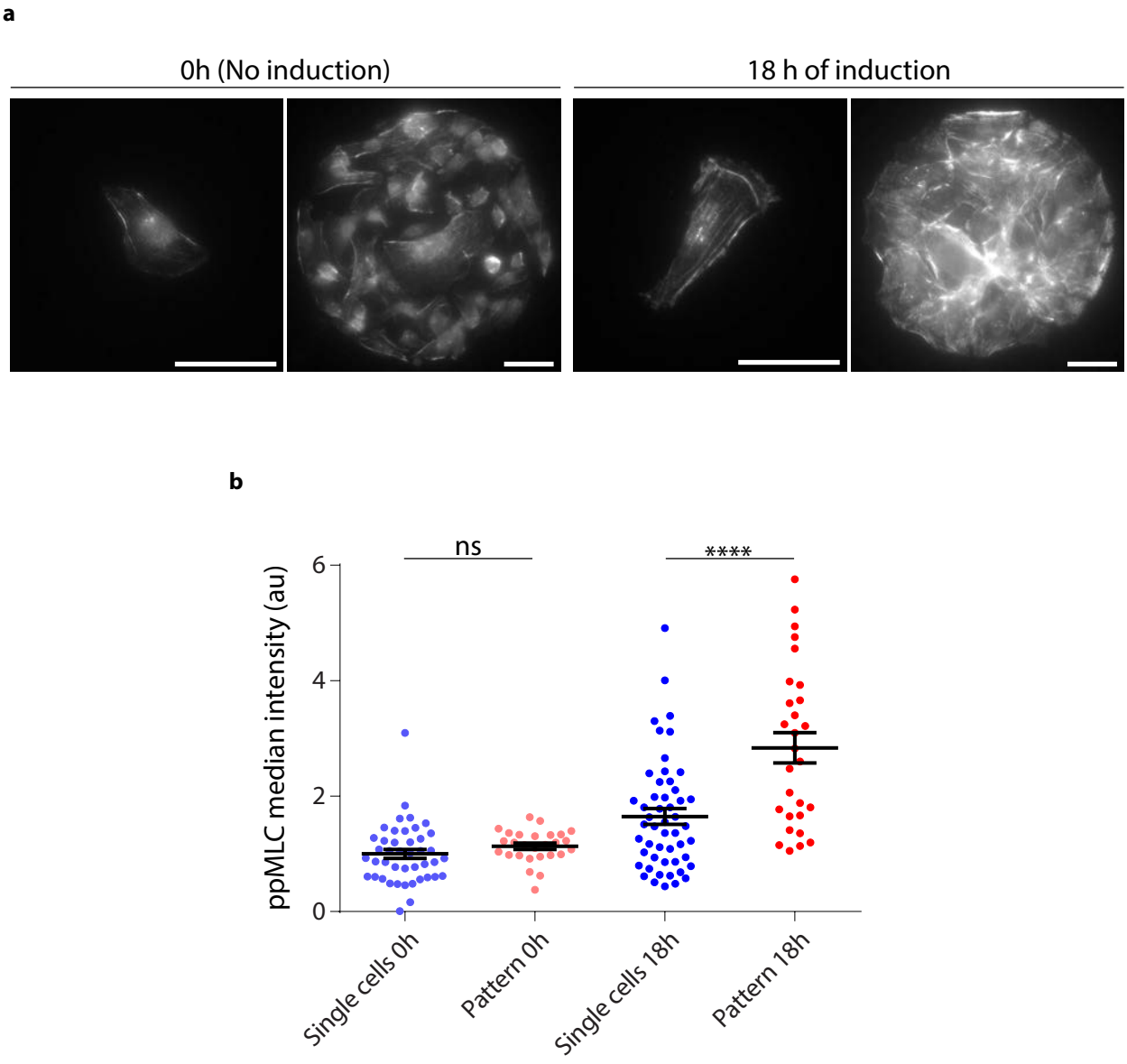

Fig. S5. Monolayers display higher levels of ppMLC than single cells upon E-cadherin induction. a, ppMLC immunostaining of single cells and cell islands before and after 18h of E-cadherin induction. Scale bar = 40 µm. **b**, Quantification of median fluorescence intensity shows that single cells and cells in monolayers start with similar levels of ppMLC. After 18h of E-cadherin induction, cell monolayers show significantly higher levels of ppMLC than single cells (Kruskal Wallis test, p-value < 0,0001). Data are presented as mean ± s.e.m. n=43 (Single cells 0h), n=27 (Pattern 0h), n=51 (Single cells 18h) and n=28 (Pattern 18h).

Supplementary figure S6

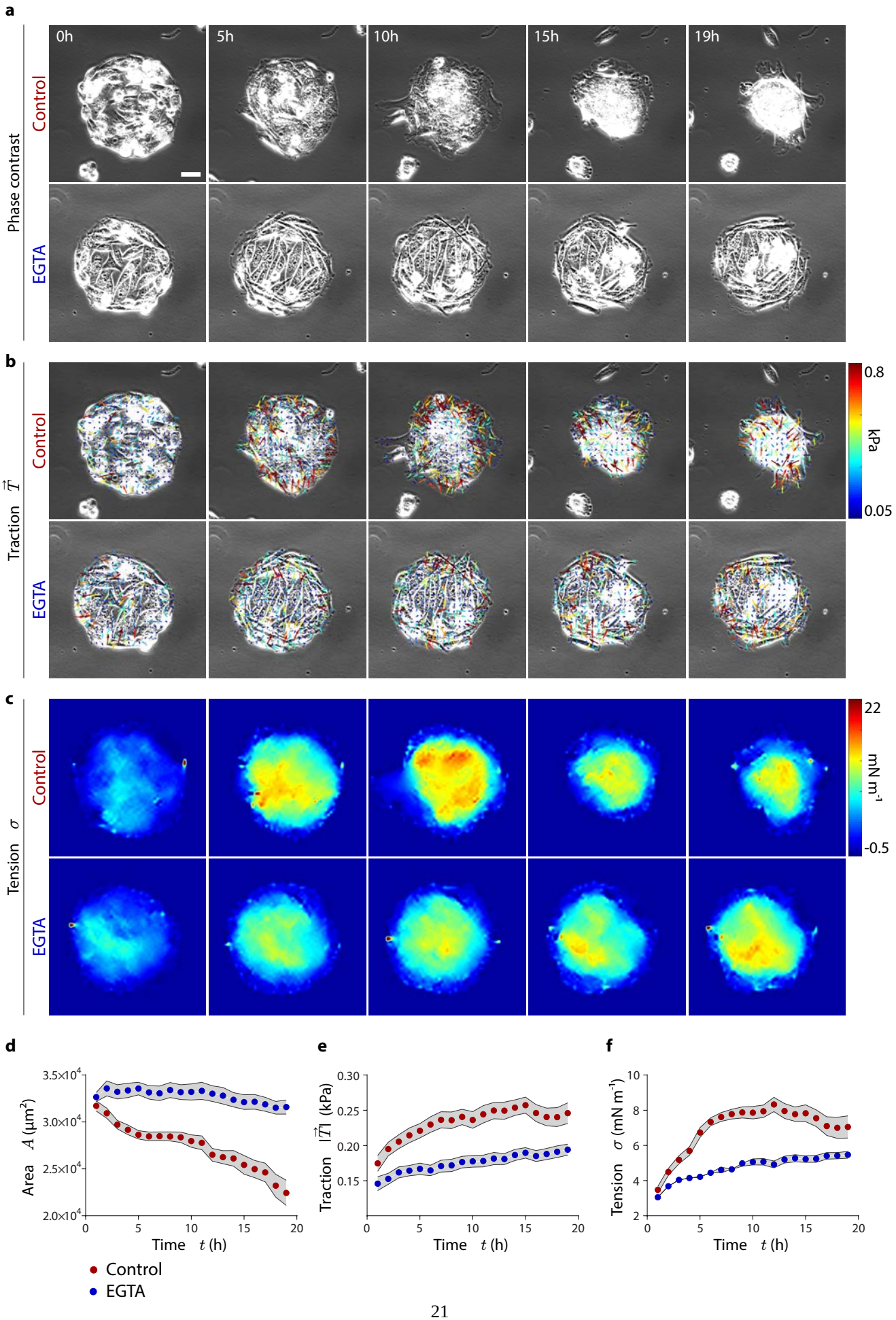

Fig S6. Calcium chelation prevents the buildup of tissue forces and the wetting transition. a-c, Phase contrast images (a), and maps of traction forces (b) and average normal monolayer tension (c) in control and EGTA treated monolayers. EGTA efficiently inhibits cell-cell junction formation, as seen from the lack of cohesiveness in the treated monolayer. **d-f**, EGTA hinders the abrupt increase in tractions (e) and tension (f) after E-cadherin induction, thereby preventing the decrease in area caused by tissue dewetting (d).

Supplementary figure S7

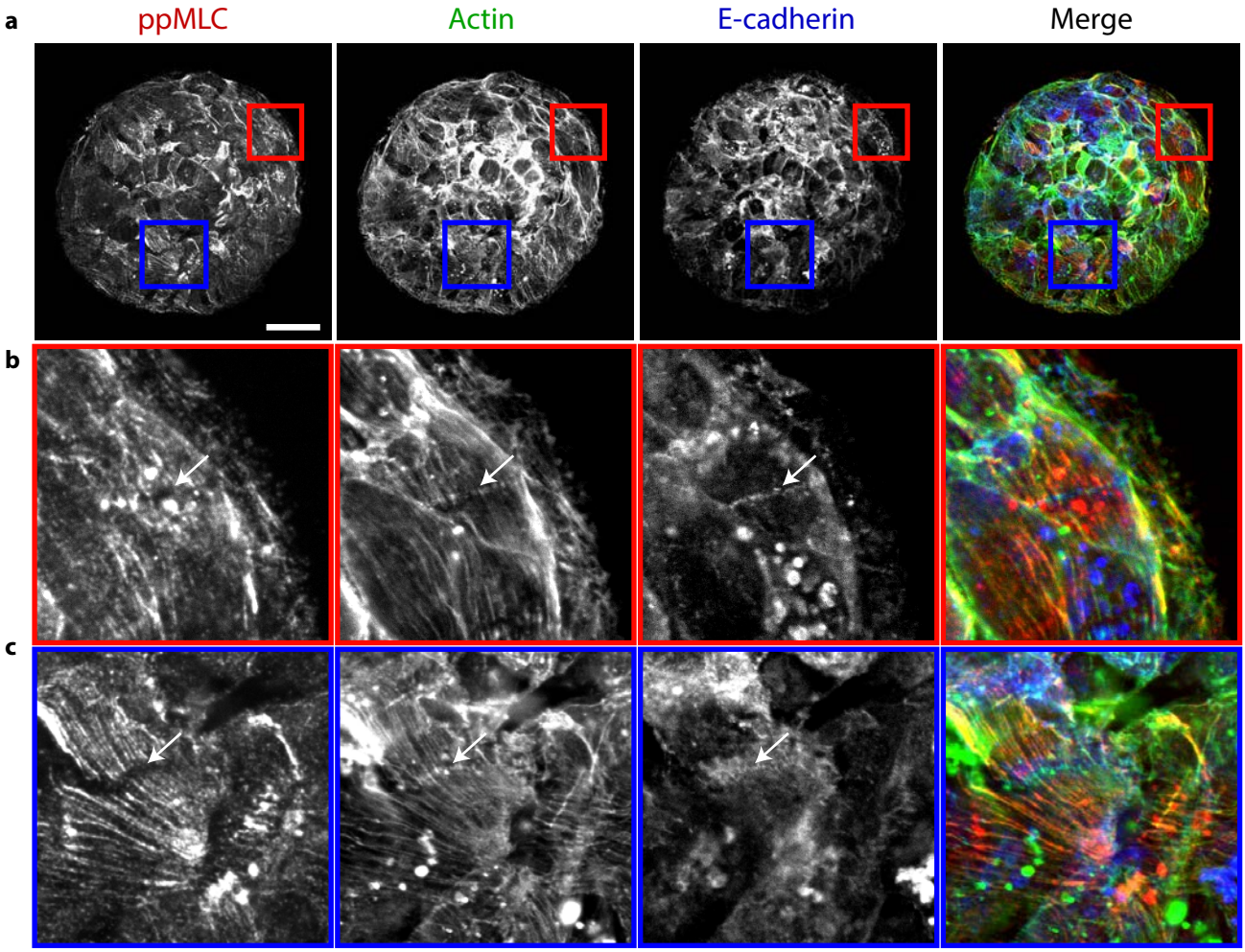

Fig S7. ppMLC accumulates at actin stress fibers but not at E-cadherin junctions. a, Immunostaining of ppMLC, Actin, and E-cadherin in cell islands after 18h of E-cadherin induction. Scale bar = 40 µm. **b,c**, Insets of the labelled regions in (a). E-cadherin junctions colocalize with actin but not with ppMLC (arrows). Instead, ppMLC accumulates at actin stress fibers.

Supplementary Figure S8

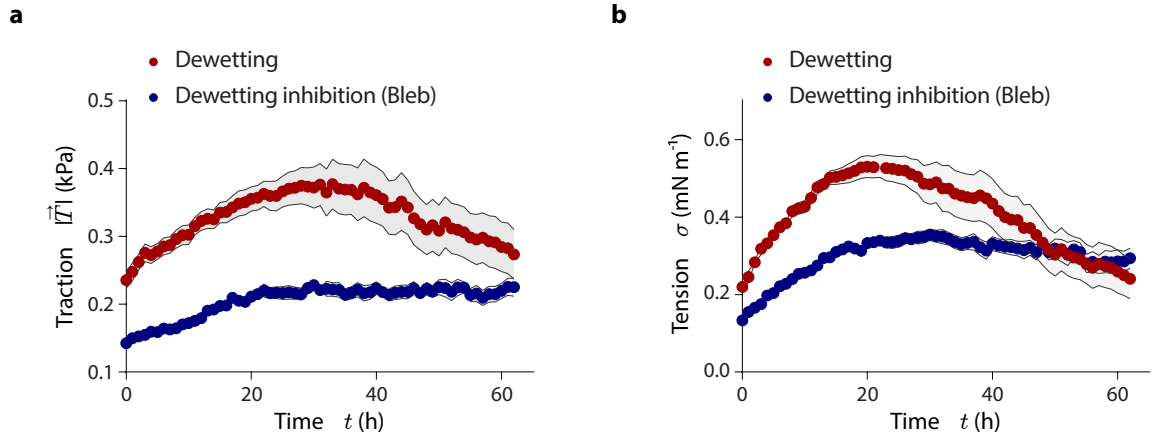

Fig. S8. Blebbistatin decreases traction forces and monolayer tension. a-b, Evolution of the average traction magnitude (a) and average monolayer tension (b) for untreated islands, and for islands treated with blebbistatin.

Supplementary figure S9

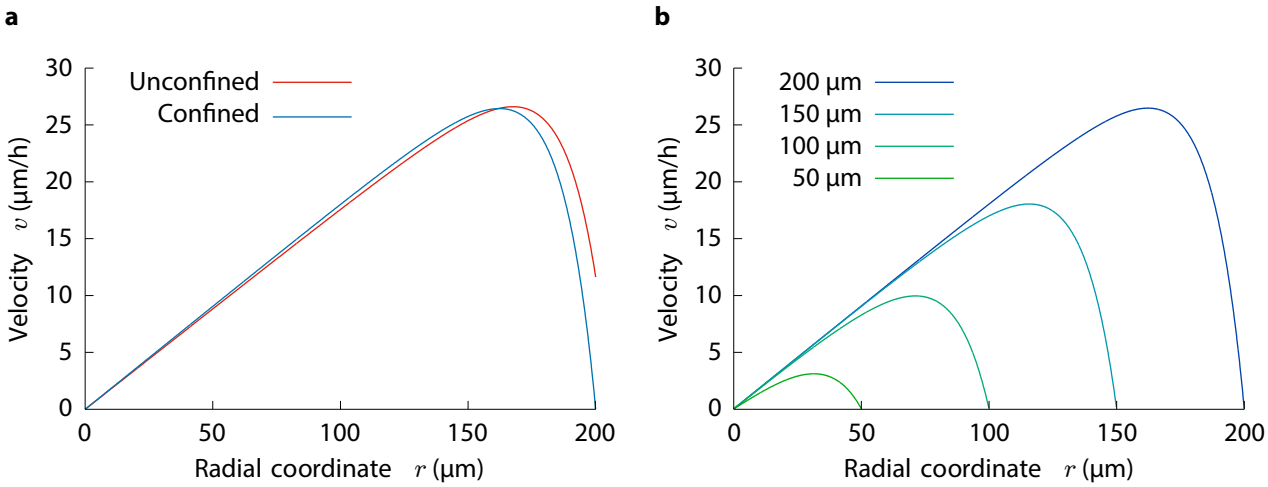

Fig. S9. Predicted velocity profiles in the monolayers. a, Velocity profile in confined and unconfined monolayers, Eq. (S22). Parameter values are T_0= 0.5 kPa, L_c = 25 µm, R = 200 µm, h = 5 µm, and η = 50 MPa·s. For the unconfined case, the contractility is -ζ = 20 kPa, under which the monolayer expands ($v(R) > 0$). For the confined case, the condition $v(R) = 0$ sets the contractility to be given by Eq. (S23). **b**, Velocity profile for monolayers of different radius. Parameter values are T_0= 0.5 kPa, L_c = 25 µm, h = 5 µm, and η = 50 MPa·s, with the critical contractility -ζ* given by Eq. (S26).

Supplementary figure S10

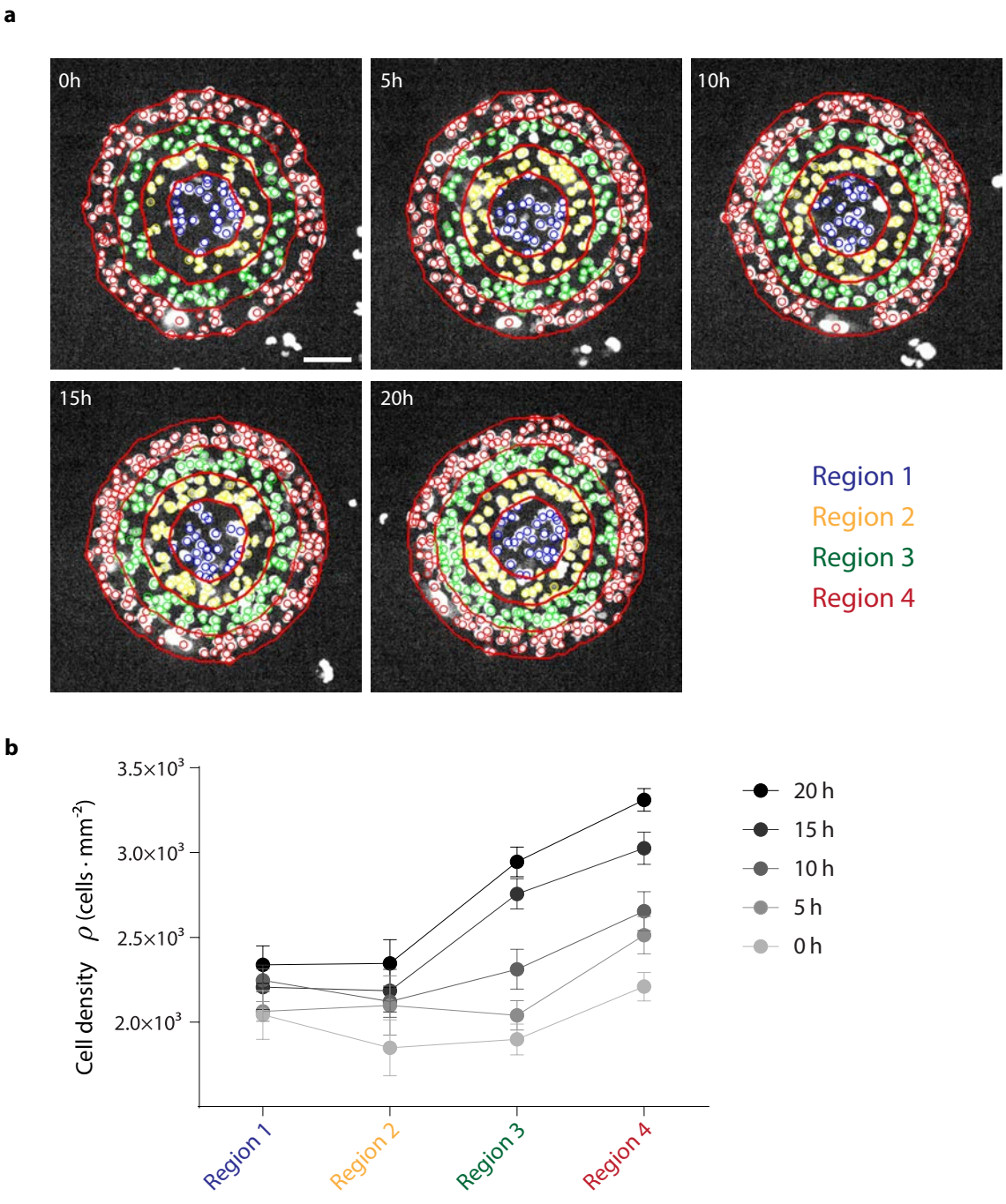

Fig. S10. Cell density increases near the monolayer edge upon induction of E-cadherin expression. a, Expression of H2B-mNeonGreen allows counting cell nuclei in concentric circular coronae. **b**, Upon induction of E-cadherin expression, the cell density profile develops a gradient towards the monolayer edge. Data are presented as mean ± s.e.m. n=5 cell islands.

Supplementary figure S11

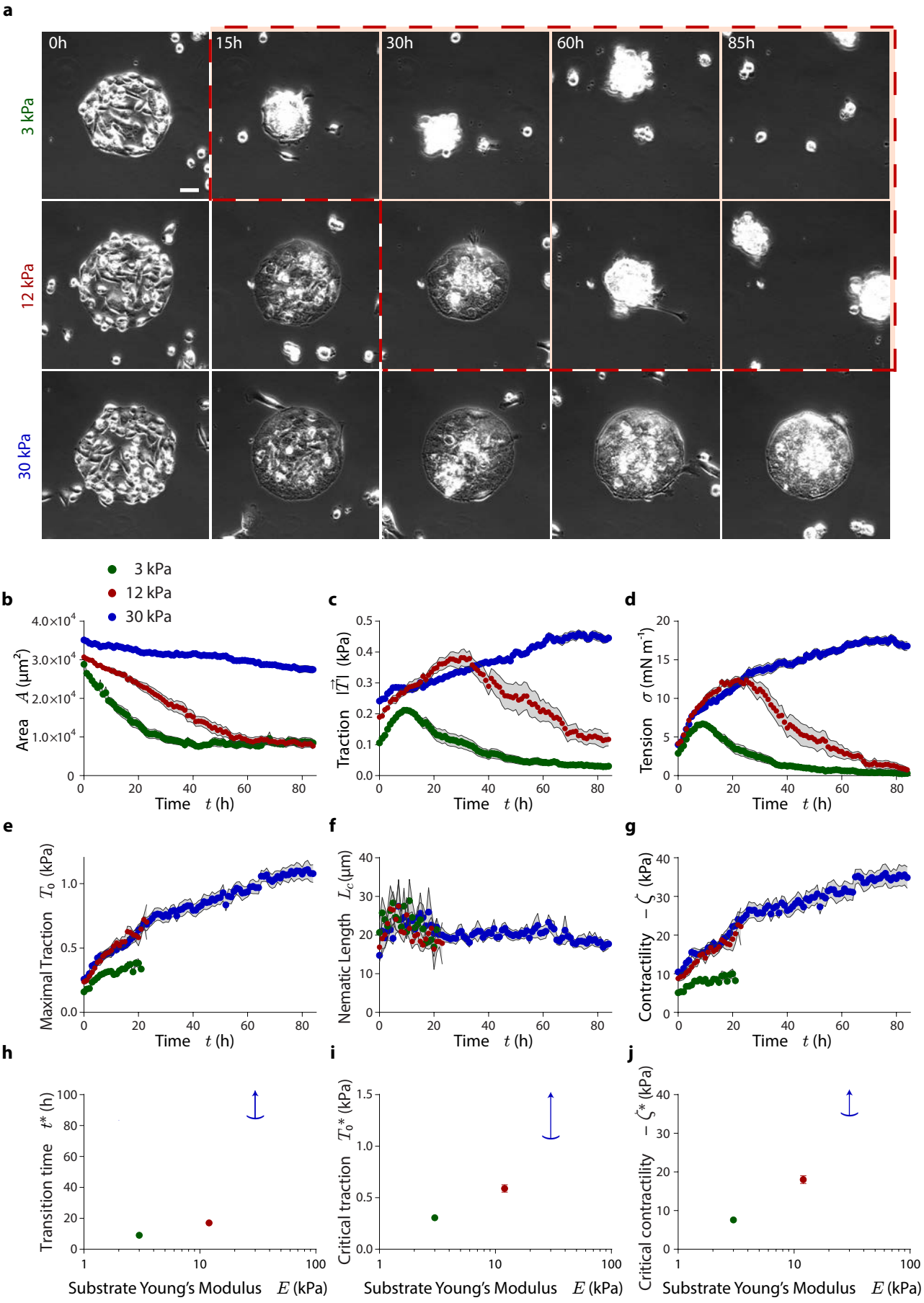

Fig. S11. The wetting transition depends on substrate stiffness. **a,** Time evolution of epithelial monolayers on substrates of different stiffness (Young's modulus of 3, 12 and 30 kPa). Monolayers on stiffer substrates dewet later (red dashed line and shade indicate dewetting). Scale bar = 40 μm. **b-d,** Evolution of monolayer area (b), mean traction magnitude (c) and average normal monolayer tension (d). **e-g,** Evolution of the maximal traction (e), nematic length (f), and contractility (g) for monolayers on substrates of different stiffness. These model parameters were obtained by fitting the model predictions to the experimental data (see Methods). **h-j**, Transition time (h), critical traction (i) and critical contractility (j) for the different substrate stiffnesses. For monolayers on 30 kPa gels, a wetting transition is not observed within the time of the experiment. Thus, critical parameter values are higher than the maximal value measured at the end of the experiment (t=84h), and hence they are indicated as open intervals (parentheses). Data are presented as mean ± s.e.m. n=23 for 3kPa gels, n=10 for 12 kPa gels and n=17 for 30 kPa gels.

Supplementary figure S12

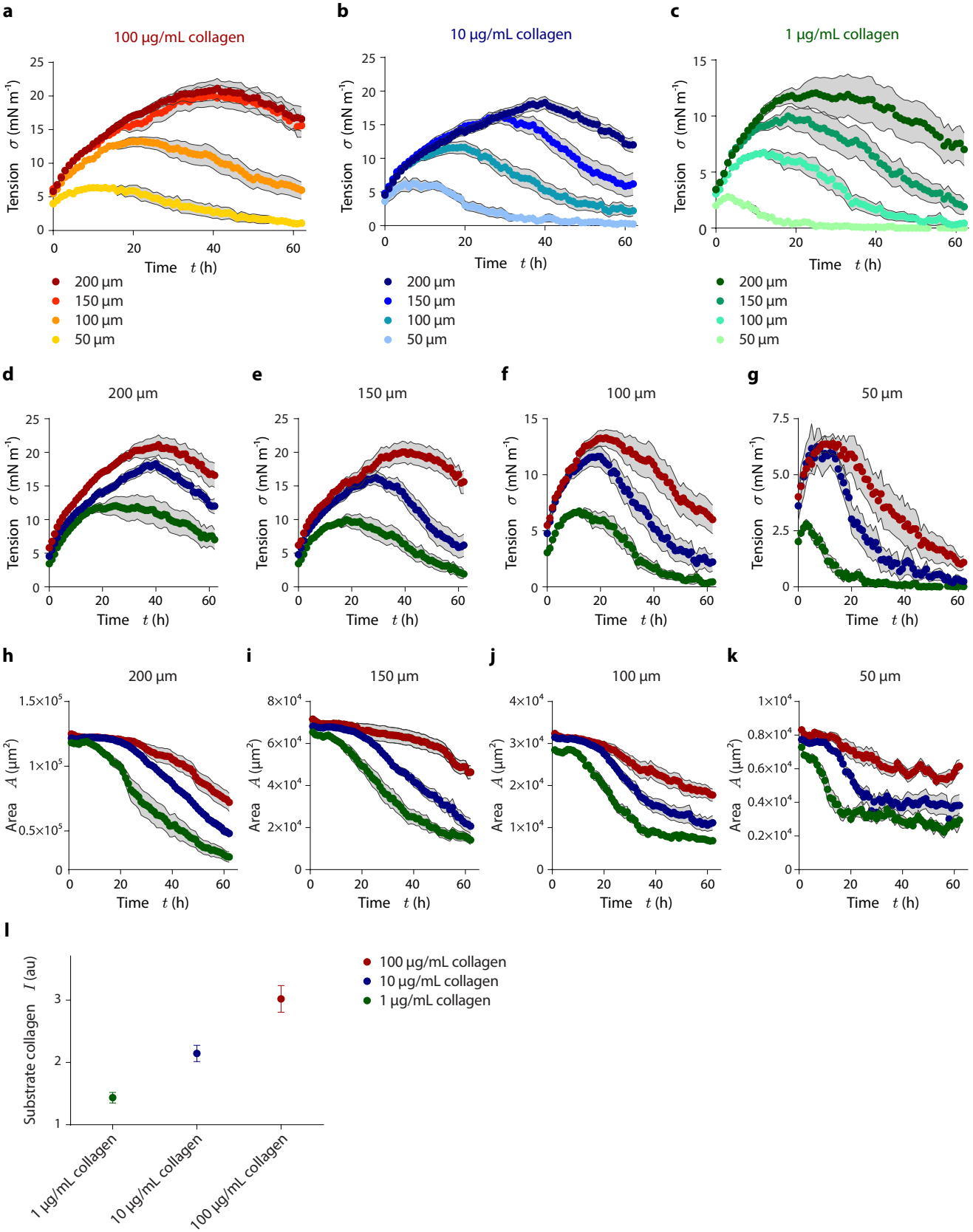

Fig. S12. Area and monolayer tension evolution in islands of different sizes and substrate ligand densities. a-c, Evolution of the average normal monolayer tension for islands of different radii on substrates of 100 μg/mL of collagen (**a**), 10 μg/mL of collagen (**b**) and 1 μg/mL of collagen (**c**). **d-g**, Evolution of the average normal monolayer tension for islands seeded on substrates with different collagen densities with radii of: 200 μm (**d**), 150 μm (**e**), 100 μm (**f**) and 50 μm (**g**). **h-k**, Evolution of the mean area for islands seeded on substrates with different collagen density with radii of: 200 μm (**h**), 150 μm (**i**), 100 μm (**j**) and 50 μm (**k**). **l**, Relative fluorescence intensity of collagen coating the substrate, quantified by immunostaining for different concentrations of collagen in solution. Data are presented as mean ± s.e.m. n=57 for 100 μg/mL of collagen; n=40 for 10 μg/mL of collagen; and n=40 for 1 μg/mL of collagen.

Supplementary figure S13

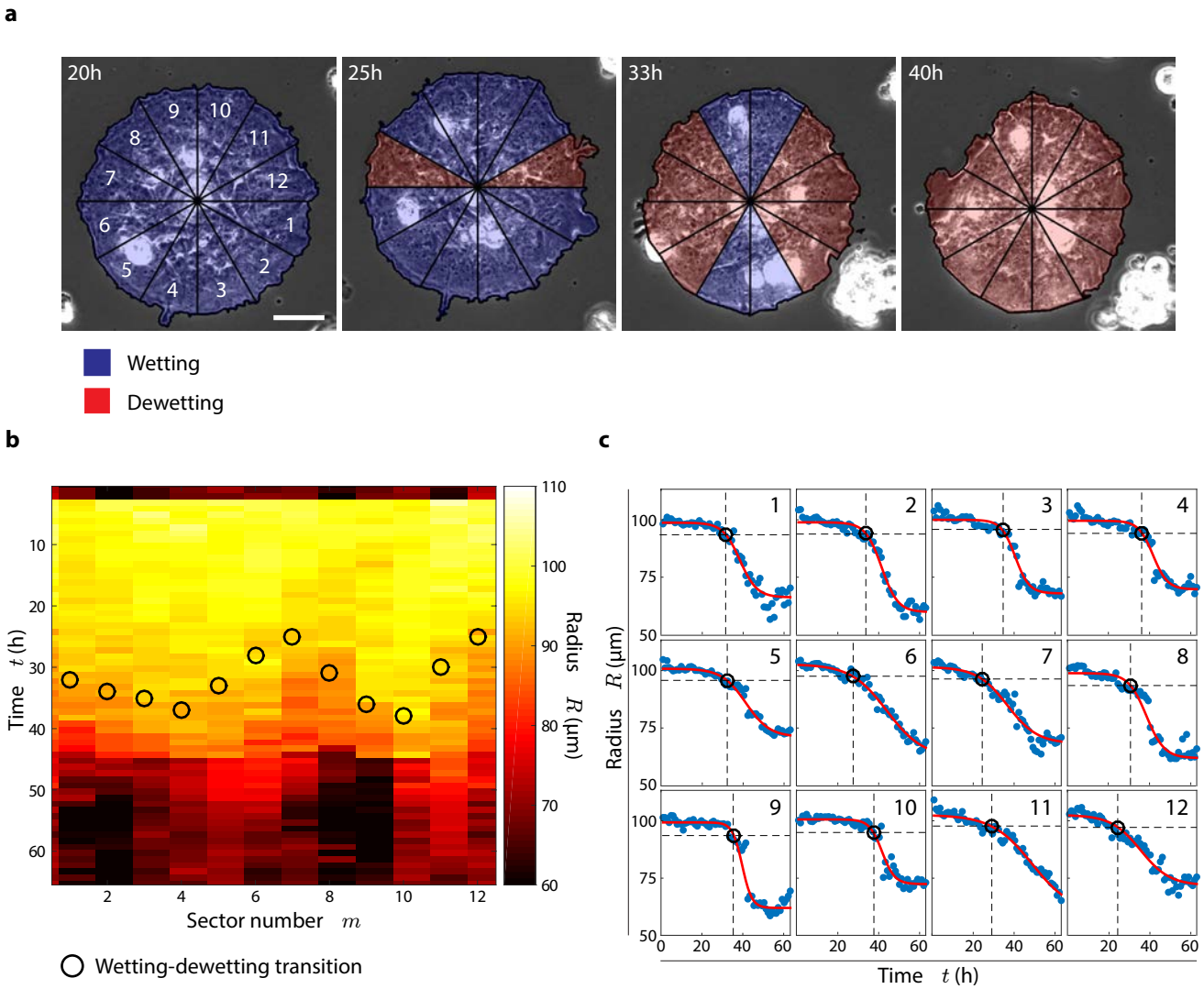

Fig. S13. User-blind criterion to determine the wetting transition time. a, Cell islands are divided in circular sectors to measure the average radius as a function of the polar angle. Blue = wetting, red = dewetting. **b**, Kymograph of the evolution of the average radius of every sector. **c**, Fit of a sigmoidal function (red line) to the evolution of the average radius of every sector (blue dots). Open circles indicate the wetting transition for each sector.

Supplementary figure S14

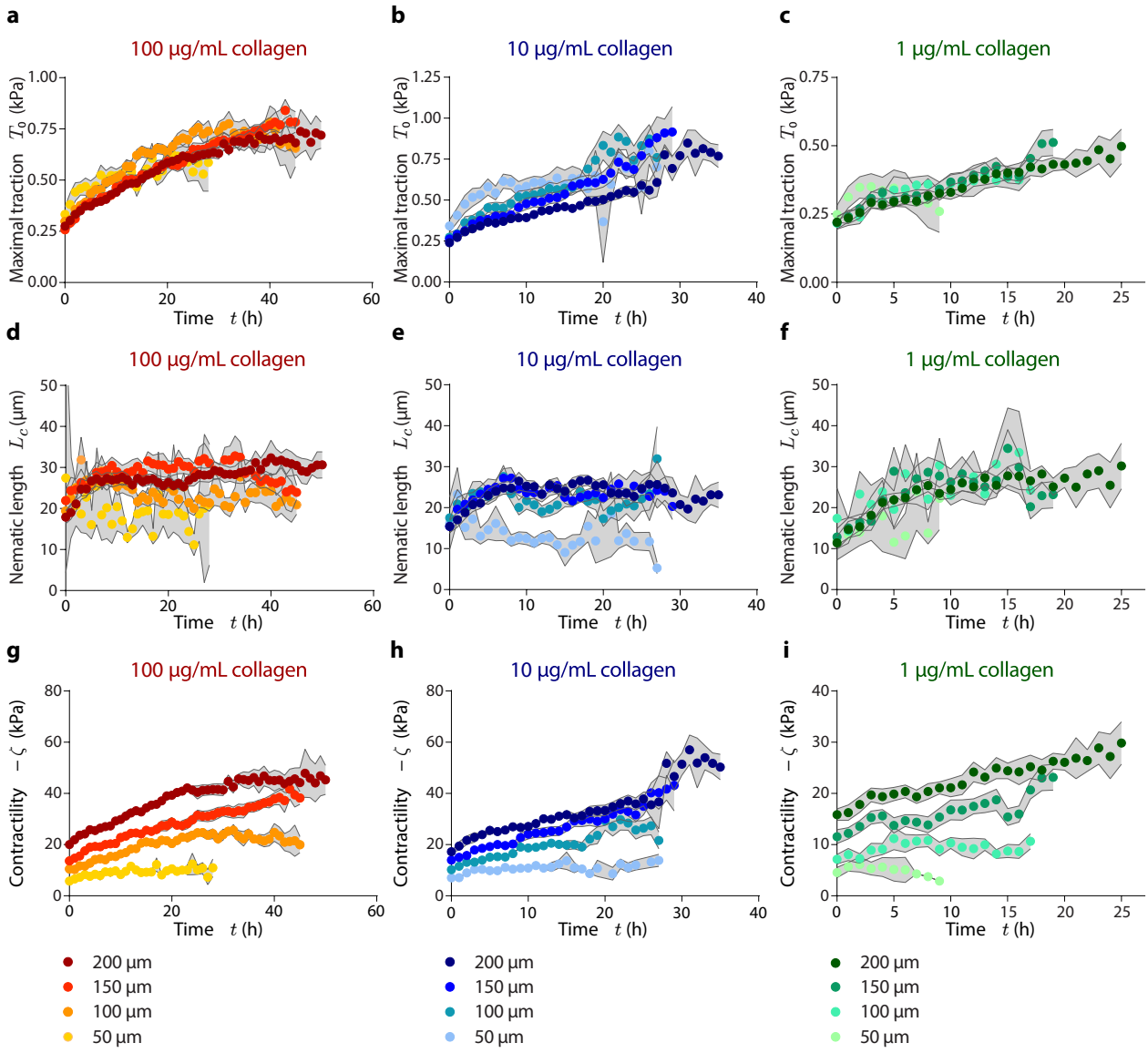

Fig. S14. Evolution of model parameters in islands of different sizes and substrate ligand densities. Evolution of the maximal traction (**a-c**), nematic length (**d-f**) and contractility (**g-i**) in islands of different radii (50, 100, 150 and 200 µm) and substrate ligand densities (100, 10 and 1 µg/mL).

Supplementary figure S15

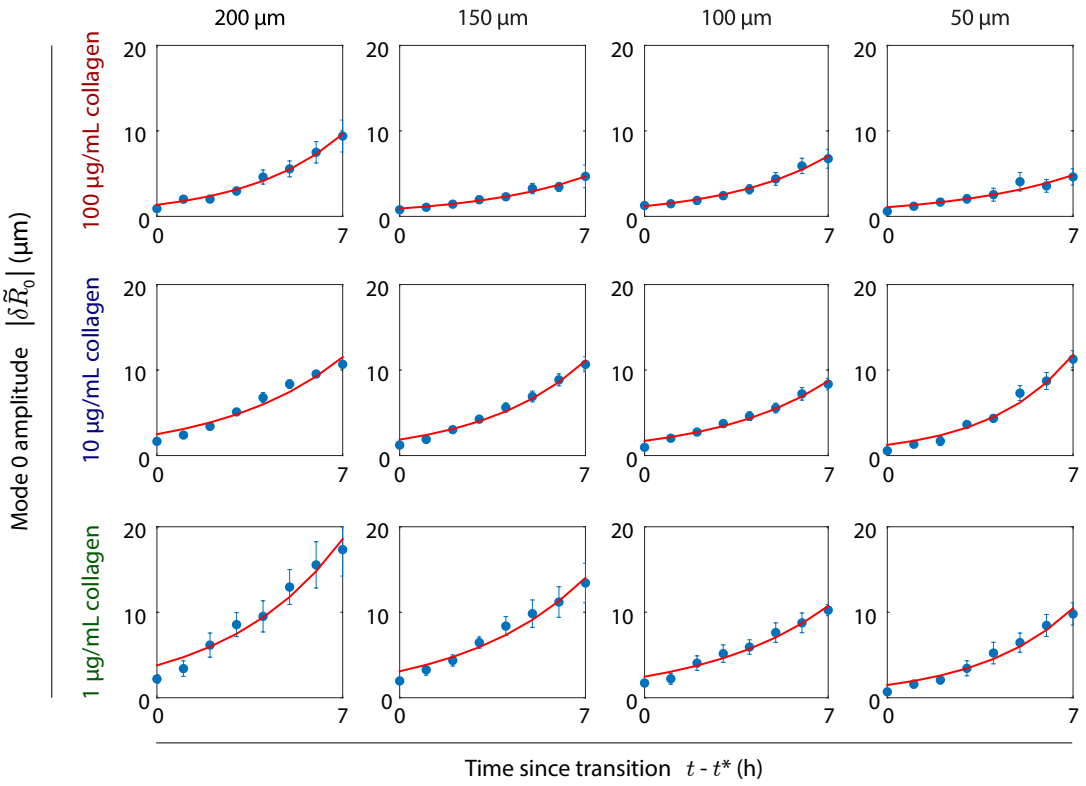

Fig. S15. Fits of the exponential growth of the perturbation mode n=0. Evolution of the average amplitude of the perturbation mode n=0 for all different monolayer radii and substrate ligand densities.

Supplementary Figure S16

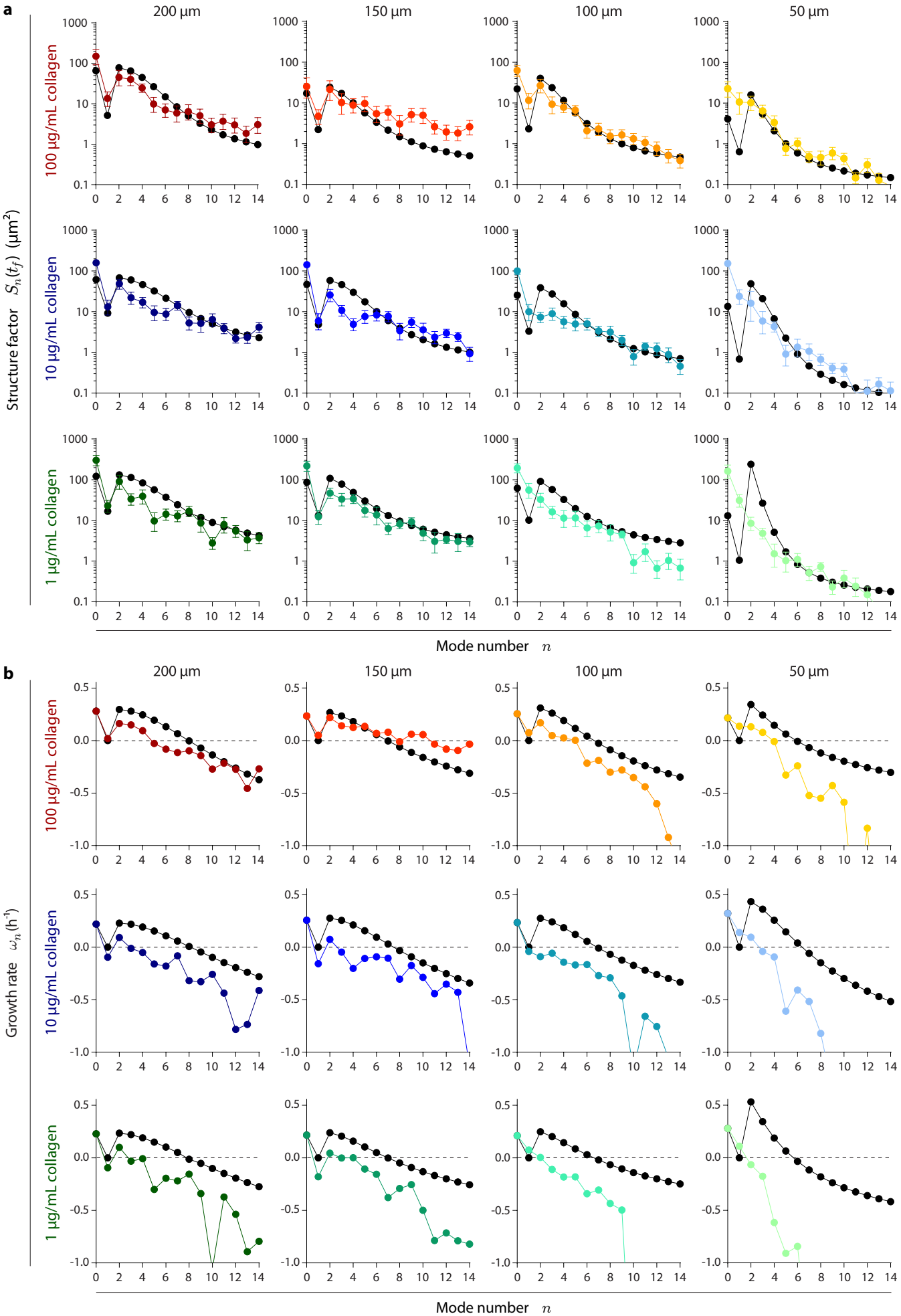

Fig. S16. Structure factors and perturbation growth rates for dewetting monolayers in islands of different sizes and substrate ligand densities. a-b, Structure factors at time $t_f - t^* = 7$ h upon the onset of dewetting (**a**) and perturbation growth rates (**b**) in islands of different radii (50, 100, 150 and 200 μm) and substrate ligand densities (100, 10 and 1 μg/mL). The predicted structure factors (Eq. 9, black symbols) are fitted to the experimental data (color symbols) to obtain the noise intensity D of perturbation mode amplitudes (see Fig. 5h). The predicted growth rates (black symbols) are compared to the experimental data (color symbols).

Supplementary Movies

Movie 1. Unconfined monolayer exhibiting a transition from wetting to dewetting. Representative example of a spreading monolayer (shown in Fig. 1f) undergoing a wetting transition. The release of confinement at t=0h allows the monolayer to freely spread. At ~25h, the monolayer spontaneously starts retracting until it collapses into a spheroidal aggregate.

Movie 2. Another example of a wetting transition in a spreading monolayer. Another spreading monolayer (shown in Supplementary Fig. 2) undergoing a wetting transition.

Movie 3. Evolution of traction and tension fields during wetting and dewetting. Videos of Phase contrast images (left), maps of traction (center) and monolayer tension (right) in a monolayer with increasing concentration of E-cadherin. A wetting transition is observed at time t=22h.

Movie 4. Orthogonal views of monolayer dewetting. Timelapse of MDA-MB-231 cells stably expressing a cell membrane marker (CAAX-iRFP). The tissue-substrate contact area decreases pronouncedly during dewetting, while the tissue evolves from a monolayer to a spheroidal cell aggregate, resembling a droplet.

Movie 5. Calcium chelation hinders the increase of tissue forces and prevents dewetting. Phase contrast, and maps of traction forces and monolayer tension of control (left) and EGTA-treated (right) cell islands. Cells treated with EGTA move individually rather than forming a cohesive monolayer, suggesting that cell-cell junctions are efficiently abrogated. In the presence of EGTA, both tractions and monolayer tension increase much more slowly than in control islands, and the wetting transition does not occur.

Movie 6. Dewetting is inhibited and reversed when tissue contractility is externally decreased. Dewetting (left), dewetting inhibition (center) and reversibility (right) assays. Partial inhibition of contractility with blebbistatin clearly delays the wetting transition. A sudden inhibition of contractility with Y27632 (t=46h) is enough to revert dewetting, inducing a rewetting of the substrate. The name of the drug indicates its presence in the cell medium.

Movie 7. Cell rearrangements in the monolayer. Phase contrast (left) and cell nuclei (right) in a 200 μm radius island during the wetting phase of the experiment. Cells incessantly exchange neighbours, a fact that provides support to the fluid behaviour of the monolayer. Moreover, cells progressively accumulate at the edge of the monolayer, which develops a gentle cell density gradient.

Movie 8. Evolution of traction and monolayer tension fields in islands of different radii. For all sizes, the magnitude of tractions and monolayer tension increase in time as E-cadherin is progressively expressed. Tractions accumulate at the edges of the monolayers, while monolayer tension has a maximum at the center. Red frames indicate monolayer dewetting.

Movie 9. Evolution of traction and monolayer tension fields in islands on substrates of different stiffnesses. For monolayer on substrates of Young's modulus 3 and 12 kPa, tissue forces increase in time, eventually triggering monolayer dewetting. This transition occurs earlier for the softest substrate. For the stiffest substrate (30 kPa), tissue forces keep increasing until the end of the experiment, suggesting that the critical contractility to induce dewetting is not reached. Red frames indicate monolayer dewetting.

Movie 10. The wetting transition time depends on tissue radius and substrate ligand density. Cell islands of different radii seeded on substrates with different substrate ligand densities exhibit the wetting transition at different times. Red frames indicate monolayer dewetting.

Movie 11. Symmetry breaking of monolayer shape during dewetting. A 200 μm radius cell island divided in 24 sectors. Blue = wetting, red = dewetting. Dewetting starts in diametrically opposed regions of the monolayer edge. Hence, the monolayer loses its initial circular shape and acquires an elliptic-like shape during the early stages of dewetting.